ACS OMEGA

http://pubs.acs.org/journal/acsodf

Article

Fabrication of TiO_2 Spheres and a Visible Light Active α-Fe_2O_3/TiO_2-Rutile/TiO_2-Anatase Heterogeneous Photocatalyst from Natural Ilmenite

Leshan Usgodaarachchi, Charitha Thambiliyagodage,* Ramanee Wijesekera, Saravanamuthu Vigneswaran,* and Murthi Kandanapitiye

Cite This: *ACS Omega* 2022, 7, 27617−27637

Read Online

ACCESS | Metrics & More | Article Recommendations | Supporting Information

ABSTRACT: High-purity (98.8%, TiO_2) rutile nanoparticles were successfully synthesized using ilmenite sand as the initial titanium source. This novel synthesis method was cost-effective and straightforward due to the absence of the traditional gravity, magnetic, electrostatic separation, ball milling, and smelting processes. Synthesized TiO_2 nanoparticles were 99% pure. Also, highly corrosive environmentally hazardous acid leachate generated during the leaching process of ilmenite sand was effectively converted into a highly efficient visible light active photocatalyst. The prepared photocatalyst system consists of anatase-TiO_2/rutile-TiO_2/Fe_2O_3 (TF-800), rutile-TiO_2/Fe_2TiO_5 (TFTO-800), and anatase-TiO_2/Fe_3O_4 (TF-450) nanocomposites, respectively. The pseudo-second-order adsorption rate of the TF-800 ternary nanocomposite was 0.126 g mg^{-1} min^{-1} in dark conditions, and a 0.044 min^{-1} visible light initial photodegradation rate was exhibited. The TFTO-800 binary nanocomposite adsorbed methylene blue (MB) following pseudo-second-order adsorption (0.224 g mg^{-1} min^{-1}) in the dark, and the rate constant for photodegradation of MB in visible light was 0.006 min^{-1}. The prepared TF-450 nanocomposite did not display excellent adsorptive and photocatalytic performances throughout the experiment period. The synthesized TF-800 and TFTO-800 were able to degrade 93.1 and 49.8% of a 100 mL, 10 ppm MB dye solution within 180 min, respectively.

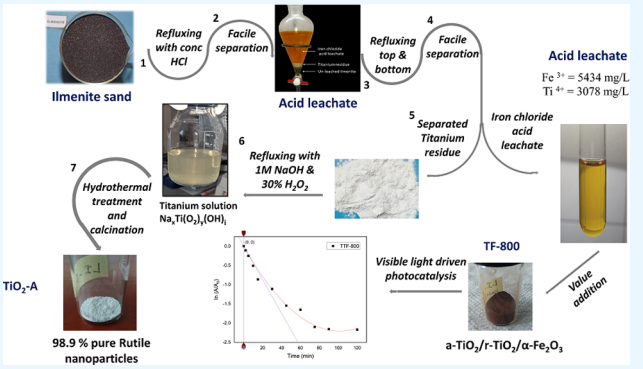

1. INTRODUCTION

The first discovery of titanium was in 1791 by the British geologist William Gregor.[1] He examined a new element in $FeTiO_3$ found in black color sand from the Helford River in England. William Gregor produced an impure white metallic oxide from $FeTiO_3$ by treatment with hydrochloric (HCl) acid followed by washing with sulfuric (H_2SO_4) acid.[2] After 119 years, pure TiO_2 was synthesized in 1910 by M.A. Hunter.[3] Globally, 50% of the titanium that is produced is used for the production of TiO_2 as white pigments, and 20 and 12% are used in paper and plastic industries, respectively.[4] The remaining 18% is used in food, medicines, toothpastes, rubber, floor coverings, and ceramics and as an additive in the cosmetics industry.[4] In recent decades, TiO_2 has been used as catalysts, dielectrics in capacitors, a functional part in some oxygen sensors, a component of surgical implants and prostheses (for bone/medical implant integration), and as a semiconductor.[2] Also, TiO_2 nanocomposites have been developed for use in solar cells and photocatalytic hydrogeneration from water.[5] TiO_2 and TiO_2 modified nanocomposites are used in advanced oxidation processes (AOPs) in water purification.[6,7]

Currently, titanium dioxide is produced from titanium ores by traditional processes such as the sulfate and chloride processes.[8,9] Globally, the sulfate process is employed in 40% of total TiO_2 production and the chloride process in 60%.[8] In the sulfate process, low-grade ilmenite (40−60%, TiO_2) or titanium slag (72−85%, TiO_2) is digested in concentrated sulfuric acid at elevated temperature and pressure. After separating the iron sulfate, the titanium liquid employed by TiO_2 is called a sulfatable titanium slag. The titanium liquid is hydrolyzed to synthesize hydrated titanium dioxide. However, the sulfate process generates huge amounts of iron sulfate byproducts, which are considered a hazardous waste. In the chloride process, either high-grade rutile or titanium slag is mixed with chlorine gas at a temperature of around 900−1000

Received: May 25, 2022
Accepted: July 14, 2022
Published: July 26, 2022

https://doi.org/10.1021/acsomega.2c03262
ACS Omega 2022, 7, 27617−27637

°C in a fluidized bed reactor in the presence of coke as a reducing agent to produce $TiCl_4$ vapor. The resulting $TiCl_4$ vapor is liquefied and converted to titanium dioxide.[10] The chloride process has advantages over the sulfate process, such as the production of high-purity TiO_2, less environmental impact, and the generation of a limited amount of hazardous waste products.[11,12] Nevertheless, the requirement of high-purity TiO_2 ore for use in the chloride process was a significant hurdle due to the inability to produce pure TiO_2 by leaching ilmenite ore. To improve ilmenite sand purity, low-grade ilmenite ores were subjected to gravity and to magnetic and electrostatic separation processes.[9,10] In general, chloride and sulfate hydrometallurgical processes can be classified as (i) a smelting process followed by either sulfuric or hydrochloric acid leaching at elevated temperatures, (ii) reduction of ilmenite followed by acid leaching, (iii) diminution of the iron content in ilmenite by oxygen and ammonium chloride, (iv) oxidation of ilmenite followed by reduction of oxidized ilmenite and hydrochloric acid leaching, and (v) roasting and magnetic separation followed by hydrochloric acid leaching.[10,13] These extractive metallurgical processes involve multiple steps of energy and high-temperature treatments over 1000 °C, making them expensive.[14] It is essential to develop an alternative process to produce high-quality TiO_2 from low-grade ores by minimizing and environmentally managing hazardous waste products.

Titanium dioxide is the most frequently applied semiconductor photocatalyst in photoinduced degradation processes. Even though TiO_2 has the disadvantage of being activated by ultraviolet (UV) light rather than visible light, it has several advantages, including being chemically and biologically inert, photocatalytically stable, and relatively easy to produce and use.[15−18] The most common polymorphs of TiO_2, rutile and anatase, exhibit band gaps (E_g) of 3.2 and 3.0 eV, respectively, and they correspond to the wavelengths of 387.45 and 413.28 nm, respectively.[19] The UV range in which light wavelengths shorter than roughly 400 nm are considered accounts for about 4% of solar radiation. Therefore, many researches have been conducted in the past to improve the photocatalytic efficiency by enhancing the visible light sensitivity such as fabrication of semiconductor heterostructures,[20] metal doping,[21,22] nonmetallic doping,[23−25] surface hybridization,[26] noble metal co-deposition,[26] and coupling with other technologies.[19,27,28] Among these methods, TiO_2 has been doped with metals including Pt,[29] Fe,[30] Cu,[31] V,[32] Cr,[33] Ag,[34] etc., and nonmetals such as C,[35] N,[36−38] and S.[37,39] Furthermore, TiO_2 has been combined with other semiconductors such as Cu_2O,[40] CdS,[41] and Bi_2S_3[41] to improve visible light photocatalytic activity by enhancing charge separation. However, the construction of heterostructures is proven to be effective to improve photoinduced charge separation and photocatalytic performance. Similarly, TiO_2 has been combined with other metal oxides such as Fe_2O_3,[42] V_2O_5,[43] CeO_2,[44] and $CoTiO_3$,[45] yielding heterojunctions in between semiconductors. In this study, we report the synthesis of an anatase-TiO_2/rutile-TiO_2/α-Fe_2O_3 heterojunction. The anatase and rutile binary heterostructure exhibited type II band alignment with the conduction band of rutile residing above that of anatase. The anatase/rutile phases allowed efficient charge separation through the photocatalyst with a minor influence on the hole recombination and strong effect on electron hole transferring. The excitation of α-Fe_2O_3 resulted due to the irradiation of visible light and electron holes migrated through the heterostructure.

The present work's significant contribution is the novel approach to produce high-purity rutile from ilmenite sand and synthesize high-purity magnetite nanoparticles based on the photocatalyst through a very effective separation technique called facile synthesis. The novel facile synthesis approach is able to utilize natural ilmenite without generating environmentally hazardous waste substances. The first key advantage of the process implemented by this work is the use of commercially available ilmenite sand as a titanium source without additional gravity, magnetic, electrostatic separation, ball milling, and smelting process, making it a straightforward and cost-effective process. The second advantage of the proposed method is that it is nonhazardous to the environment unlike existing hydrometallurgical methods due to effectively converting the byproduct iron-based hydrochloric acid leachate to an efficient photocatalyst. The photocatalyst recovery process makes an extraordinary contribution to a greener environment by effective conversion and use of highly corrosive iron-based hydrochloric acid leachate.

2. MATERIALS AND METHODS

2.1. Chemicals. Ilmenite sand of particle size 100−200 μm was supplied by Lanka Mineral Sand (pvt) Ltd. Hydrochloric acid (37%, HCl), sodium hydroxide (98%, NaOH), and ethanol (99.95%, C_2H_5OH) were purchased from Sigma-Aldrich USA. Ethylene diamine tetraacetic acid (EDTA), isopropyl alcohol (IPA), and sodium persulfate (PS) were purchased from Sigma-Aldrich, GmbH. Hydrogen peroxide (30%, H_2O_2) and ammonium hydroxide (29%, NH_4OH) were purchased from Merck KGaA USA. Ferrous sulfate heptahydrate (99.5%, $FeSO_4{\cdot}7H_2O$) and cetyltrimethylammonium bromide (100%, $C_{19}H_{42}BrN$) were purchased from Sisco Research Laboratories in India. All reagents used were of analytical grade. Solutions were prepared using ultra-pure water.

2.2. Hydrochloric Acid Leaching and Facile Separation. Ilmenite sand was washed thoroughly with ultra-pure water to completely remove dirt, dust, and suspended salts followed by drying at 80 °C. Dried ilmenite (12 g) was leached in 200 mL of concentrated HCl acid under vigorous stirring at 110 °C for 6 h under refluxing. The leached slurry was allowed to cool down and settle into layers in a solid−liquid separation funnel. The unleached ilmenite and titanium residue was separated and subjected to a second leaching cycle with 200 mL of concentrated hydrochloric acid at 110 °C for 6 h, and the slurry was allowed to settle into layers. This procedure was repeated three more times using 100 mL of concentrated HCl acid. Leachates produced after each cycle were combined, and oxygen gas was bubbled through overnight at 1 bar pressure to completely oxidize ferrous ions to ferric ions. The homogenized mixture was filtered through a Whatman filter paper, and the filtrate and the solid residue were collected separately. The leachate was analyzed by ICP-MS analysis. Minor quantities of unreacted ilmenite extracted into titanium residue during the solid−liquid separation were completely evacuated by further refluxing in 200 mL of 6 M HCl acid at 110 °C for 4 h under vigorous stirring. The resulting slurry was filtered, and sediment residue was thoroughly washed with ultra-pure water and 2-proponol until free from acid and chloride ions. Afterward, it was dried at 80 °C.

https://doi.org/10.1021/acsomega.2c03262
ACS Omega 2022, 7, 27617−27637

2.3. Preparation of Nanomaterials. *2.3.1. Synthesis of TiO_2 Nanoparticles.* Dried titanium solid (3 g) residue was placed in a round-bottom flask, and 120 mL of 1 M NaOH solution was added. Afterward, 2 mL of 30% H_2O_2 was added as an oxidizing reagent, and the slurry was condensed at 40 °C for 1 h under reflux. The resulting mixture was centrifuged for 30 min at 6500 rpm, and the supernatant and precipitate were collected separately. The yellowish-green supernatant was called sodium titanate liquor, and it was divided into an equal volume of two portions. The first portion of sodium titanate liquor was treated hydrothermally at 180 °C for 2 h. The resulting white dispersion was further diluted with acidified deionized water. The resultant white color dispersion was filtered using a Whatman cellulose nitrate membrane filter paper, and the sedimented residue was thoroughly washed with ultra-pure water and ethanol until the washings are free of hydroxide ions. The successful elimination of hydroxy ions was confirmed by measuring pH. The resulting powder was dried at 80 °C and calcined at 800 °C to obtain TiO_2 nanoparticles. This material is referred to as TiO_2-A.

Similarly, to understand the formation of a porous structure during the synthesis of TiO_2, cetyl trimethyl ammonium bromide (CTAB) was introduced as the structure-directing agent. CTAB was gently dissolved in a 1:1 (v/v) mixture of ethanol and water. The conductivity of ethanol and water mixture was measured during the addition of CTAB. The addition of CTAB into the water−ethanol mixture took place until the conductivity of the solution became constant. The second portion of sodium titanate liquor was added dropwise into the CTAB solution and homogenized for 30 min. This mixture was treated hydrothermally at 180 °C for 2 h. The residue was isolated in the same manner described above for the synthesis of TiO_2 without CTAB. This material is referred to as TiO_2-B.

2.3.2. Synthesis of TiO_2/Fe_2TiO_5 Based Nanocomposites. Concentrated ammonium hydroxide was added dropwise to the leachate obtained by acid digestion of ilmenite under vigorous stirring until the pH of the reaction mixture reached 10. The resultant brown color slurry was aged for 12 h and washed thoroughly with ultra-pure water until the washings were free from chloride ions and the solution became neutral. Dried powder (TFTO) was calcined at 800 °C. This prepared powder is referred to as TFTO-800.

2.3.3. Preparation of TiO_2/Fe_3O_4 and TiO_2/Fe_2O_3 Based Nanocomposites. Oxygen gas was bubbled through the leachate that was obtained from the acid digestion of ilmenite. The obtained solution was transferred to a two-neck round-bottom flask, and nitrogen gas was bubbled into the reaction mixture for 1 h. Then, 0.0237 mol of $FeSO_4{\cdot}7H_2O$ was added to the reaction mixture in a nitrogen atmosphere. After the complete dissolution of $FeSO_4{\cdot}7H_2O$, ammonium hydroxide was added dropwise under vigorous stirring. Nitrogen gas was bubbled continuously until the pH of the reaction mixture reached 10. The resultant black slurry was aged for 12 h and thoroughly washed with ultra-pure water until the washings were free from chloride ions and neutral. The dried black color powder was calcined at 450 and 800 °C, separately. The uncalcined powder is referred to as TF, and samples calcined at 450 and 800 °C are referred to as TF-450 and TF-800, respectively.

2.4. Material Characterization. The crystalline structure of the synthesized samples was examined by an Advanced Bruker system X-ray diffraction (XRD) diffractometer. The X-rays were generated at 30 mA current and 40 kV voltage equipped with a Cu Kα anode. The diffractograms were generated by scanning in the 2θ range of 5−80° with a 2°/min scanning rate. The samples were analyzed with X'Pert High Score Plus (PANalytical). The average crystalline size of the nanoparticles was calculated by the Debye−Scherrer equation (eq 1).

$$D = \frac{0.9\lambda}{\beta \cos\theta} \tag{1}$$

where λ is the wavelength of Cu Kα (1.54060 nm), θ is the diffraction angle, and β is the full width at half-maximum in radians.

The chemical composition of the samples was analyzed by HORIBA Scientific XGT-5200 X-ray fluorescence (XRF). The morphology and particle size of the prepared nanoparticles were characterized by a Zeiss field emission scanning electron microscope (FE-SEM) and transmission electron microscope (TEM). A FEI Tecnai F20 Super-Twin equipped with an FEG source (200 kV) was used to examine the TEM morphology of the produced nanocomposites. An Oxford Instruments energy dispersive X-ray (EDX) was used to acquire EDX spectra. The particle size distribution and the average particle size were determined by the ImageJ software. The nitrogen sorption isotherms of the TiO_2 samples were obtained at 77 K using a Quantachrome Autosorb IQ Station 1 analyzer. The samples were dried under a vacuum for 12 h at 393 K before performing the analysis. The ultraviolet−visible diffuse reflectance (UV−vis DRS) of the prepared samples were measured using a Shimadzu 1800 UV/Visible spectrophotometer utilizing a precision Czerny−Turner optical system. The absorbance of MB samples was acquired by a Shimadzu UV-1990 double beam UV−visible spectrophotometer.

2.5. Photocatalytic Measurements. The photocatalytic performance of the synthesized catalysts was evaluated under irradiation generated by a 50 W visible light LED source. In a typical photocatalytic experiment, 200 mg of the photocatalyst (TFTO-800, TF-450, and TF-800) was immersed in 100 mL (10 mg/L) of methylene blue dye solution (MB). Photocatalysts were shaken in the MB solution under dark conditions till adsorption−desorption equilibrium was reached. During the dark adsorption, aliquots were withdrawn at specific times to measure the absorbance readings. The mixture was then exposed to the LED light source, and aliquots were withdrawn at specific time intervals. The absorption spectra were obtained after necessary dilution using a Shimadzu UV-1900 UV−visible spectrophotometer, and maximum absorbance was recorded at 665 nm. Similar to this, the effects of sacrificial agents were investigated using the sacrificial agents IPA, EDTA, and PS. The concentration of the sacrificial agents was maintained at 8 mmol in a 100 mL solution of 10 mg/L MB. Using a Shimadzu UV-1900 UV−visible spectrophotometer, the absorption spectra were acquired following the appropriate dilution and maximum absorbance recorded in 665 nm.

3. RESULTS AND DISCUSSION

3.1. Precipitation of the Rutile Nanoparticles and Photocatalyst Composites. Ilmenite sand was directly digested in concentrated hydrochloric acid as expressed in eqs 2 and 3.[46] Dissolution of iron is prominent at low ratios of acid to ilmenite, while at high ratios, efficient dissolution of

https://doi.org/10.1021/acsomega.2c03262
ACS Omega 2022, 7, 27617−27637

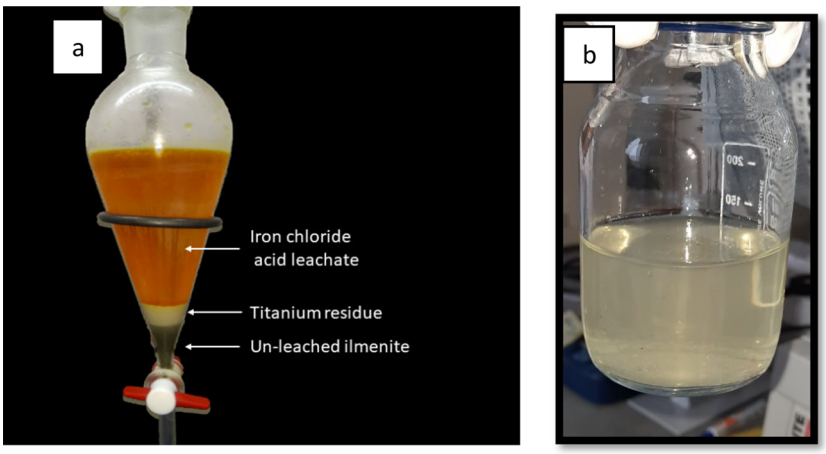

Figure 1. (a) Facilely separated unreacted ilmenite, leached titanium residue, and leached iron chloride with other metallic chlorides and (b) $Na_xTi(O_2)_y(OH)_j$ titanium solution (titanium-sol).

both iron and titanium was obtained.[47] Ilmenite sand was acid leached in five continuous cycles. After each leaching cycle, unreacted ilmenite sand, titanium residue, and acid leachate were separated by a solid–liquid separation technique. As shown in Figure 1a unleached ilmenite settled at the bottom of the funnel, while the leached titanium residue remained in between the aqueous acid leachate and the denser unleached ilmenite layer. Less titanium residue was produced after the first leaching cycle with a highly intense orange color leachate. The color of the leachate decreased with increasing number of the cycle and turned out to be more yellow by the end of the fifth cycle. This suggests that during the first few cycles, more iron was leached out with titanium, while during latter leaching cycles, predominantly titanium leached out with less iron. This is due to the fact that loosely bound iron tends to leach out more easily rather than breaking the stable lattice, which limits the dissolution of titanium.

The white-colored titanium residue solid layer that was obtained is a combination of the precipitated hydrolyzed TiO_2 in the form of $TiO_2{\cdot}nH_2O$ and H_2TiO_3 according to eqs 4 and 5.[46] However, the condensation reaction of H_2TiO_3 had taken place during the washing and drying process of titanium residue which yields to unstable H_2TiO_3.[48]

$$FeTiO_3 + 4HCl \rightarrow Fe^{2+} + TiOCl_4^{2-} + 2H_2O \quad (2)$$

$$FeTiO_3 + 4HCl \rightarrow FeCl_2 + TiOCl_2 + 2H_2O \quad (3)$$

$$TiOCl_4^{2-} + (1+n)H_2O \rightarrow TiO_2{\cdot}nH_2O + 2H^+ + 4Cl^- \quad (4)$$

$$TiOCl_2 + 2H_2O \rightarrow H_2TiO_3 + 2HCl \quad (5)$$

Ilmenite sand consists of a variety of minerals. Hence, the leaching process of the ilmenite with hydrochloric acid was a complex heterogeneous reaction. The white titanium residue synthesized by the hydrochloric acid leaching process suggested the complete separation of pure titanium products by removing iron. However, the presence of quartz, anorthite, and aluminum phosphate in the titanium residue significantly affects the purity of synthetic rutile. It is well-known that titanium peroxide gel $Ti(OH)_2O_2$ forms in a reaction of metallic Ti with H_2O_2.[49] The titanium peroxide gel that is produced decomposes into an amorphous hydrate titania $TiO_2{\cdot}nH_2O$ layer.[49]

Similarly, to increase the purity of synthesized rutile in this study, the titanium residue was treated in a mild alkaline condition using NaOH with H_2O_2. The presence of H_2O_2 is necessary for the formation of high-purity amorphous TiO_2 nanoparticles. As shown in eq 6, under an alkaline environment, the hydrated titania layer may react with NaOH to form $NaHTiO_3$.[50] The $NaHTiO_3$ that is formed is expected to be transformed into $Na_xTi(O_2)_y(OH)_j$ via the condensation reactions shown in eqs 7–9.[46] The synthesized $Na_xTi(O_2)_y(OH)_j$ is transferred to $H_2Ti_3O_7$ when diluted in deionized water.[14] $H_2Ti_3O_7$ converts into rutile TiO_2 upon calcination at 800 °C according to eq 10.

$$TiO_2{\cdot}nH_2O + NaOH \rightarrow NaHTiO_3 + nH_2O \quad (6)$$

$$NaHTiO_3 + H_2O_2 \rightarrow Na_xTi(O_2)_y(OH)_j \quad (7)$$

$$TiO_2{\cdot}nH_2O + H_2O_2 + NaOH \rightarrow Na_xTi(O_2)_y(OH)_j \quad (8)$$

$$H_2TiO_3{\cdot}nH_2O + H_2O_2 + NaOH \rightarrow Na_xTi(O_2)_y(OH)_j \quad (9)$$

$$H_2Ti_3O_7 \rightarrow 3TiO_2 + H_2O \quad (10)$$

During the formation of $Na_xTi(O_2)_y(OH)_j$, silica and other impurities remained undissolved.[46] As shown in Figure 1b, $Na_xTi(O_2)_y(OH)_j$ was a greenish-yellow solution named titanium solution (titanium-sol), and it was used to synthesize rutile nanoparticles. Titanium-sol was directly subjected to the hydrothermal treatment at 180 °C for 2 h to synthesize amorphous titanium followed by calcination at 800 °C to synthesize rutile nanoparticles (TiO_2-A). TiO_2-B was synthesized by adding titanium-sol into CTAB dropwise and hydrothermally treating the product followed by calcination at 800 °C.

One of the key novel outcomes of this synthesis method is the ease in which valuable photocatalysts (TF-450, TF-800, and TFTO-800) were produced, which were synthesized effectively by utilizing environmentally hazardous iron-rich acid leachate. TF-450 composed of the anatase phase of TiO_2 and Fe_3O_4 is magnetically separable. Also, TF-800 is not magnetically separable as it consists of a mixture of anatase and rutile phases of TiO_2 with α-Fe_2O_3. The acid leachate obtained after the acid digestion of ilmenite contains iron in ferrous

https://doi.org/10.1021/acsomega.2c03262
ACS Omega 2022, 7, 27617–27637

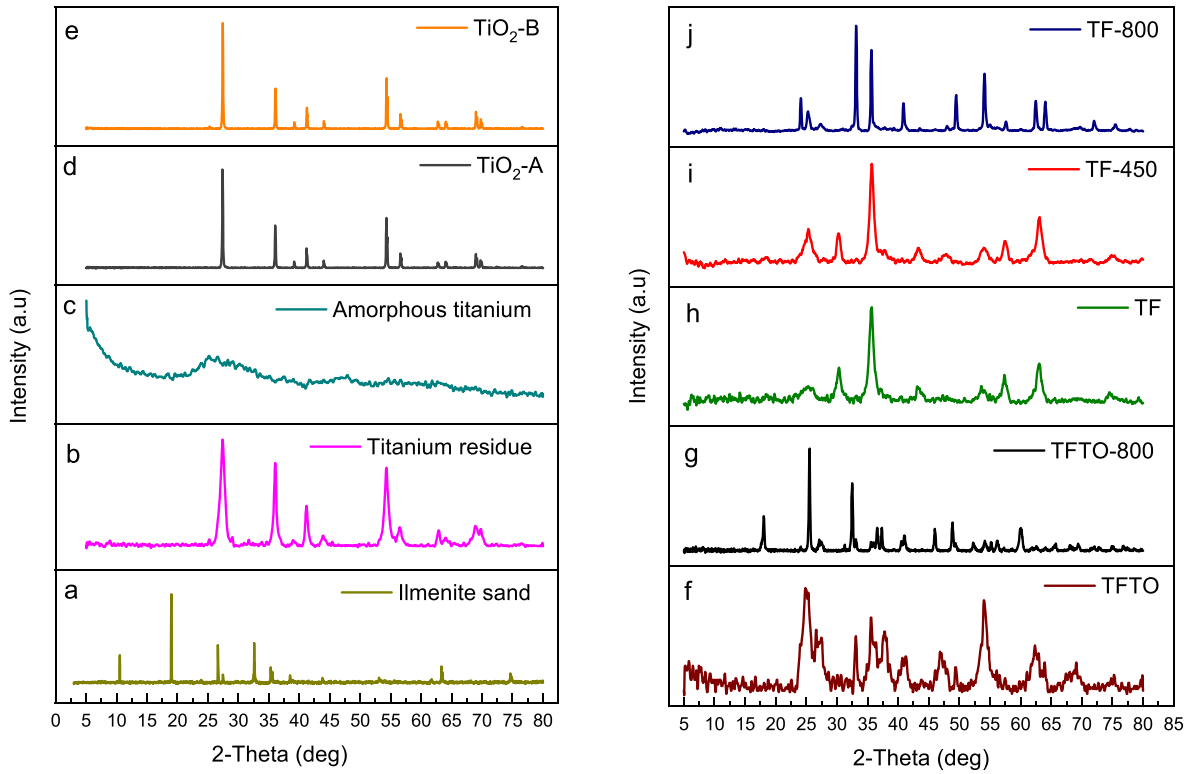

Figure 2. XRD pattern of the (a) natural ilmenite, (b) dried titanium residue, (c) amorphous titanium dried at 100 °C, (d) TiO_2-A, (e) TiO_2-B, (f) uncalcined TFTO composite, (g) TFTO-800 composite, (h) TF composite, (i) TF-450 composite, and (j) TF-800 composite.

Table 1. Chemical Composition of the Ilmenite Sand as Metallic Oxides

material	Al_2O_3 (%)	V_2O_5 (%)	SiO_2 (%)	P_2O_5 (%)	K_2O (%)	CaO (%)	TiO_2 (%)	Cr_2O_3 (%)	MnO_2 (%)	FeO (%)	ZnO (%)	ZrO_2 (%)
Ilmenite	1.02	1.21	3.94	0.04	0.08	0.61	48.87	0.15	0.87	42.81	0.08	0.15
TiO_2-A		1.22					98.78					
TiO_2-B		1.06					98.94					

(Fe^{2+}) and ferric (Fe^{3+}) forms in addition to the Ti^{4+}. However, it is virtually impossible to determine the exact Fe^{2+} and Fe^{3+} ion concentration of acid leachate as Fe^{2+} readily oxidizes to Fe^{3+} in the presence of O_2 dissolved in the medium and that is present in the atmosphere as shown in eq 11. The molar ratio of Fe^{2+} and Fe^{3+} was very important in determining the magnetism of the synthesized magnetite nanoparticles.[51] Therefore, to completely oxidize Fe^{2+} to Fe^{3+}, oxygen gas was bubbled through the acid leachate, and the resulting solution contained Fe^{3+} as $FeCl_3$ and Ti^{4+} present as H_2TiOCl_4 or $TiOCl_2$. The total Fe^{3+} and Ti^{4+} concentrations were determined by ICP-MS and were found to be 5434 and 3078 mg/L, respectively. Then $FeSO_4{\cdot}7H_2O$ was added to the acid leachate being half in number of moles of Fe^{3+} while nitrogen gas bubbling. The precipitation of Fe_3O_4 nanoparticles and $Ti(OH)_4$ by the addition of NH_4OH can be expressed according to eqs 12−17.

$$4Fe^{2+} + O_2 + 4H^+ \rightarrow 4Fe^{3+} + 2H_2O \quad (11)$$

$$Fe^{2+} + 2OH^- \rightarrow Fe(OH)_2 \quad (12)$$

$$Fe^{3+} + 3\,OH^- \rightarrow Fe(OH)_3 \quad (13)$$

$$Fe(OH)_3 \rightarrow \alpha - FeOOH + H_2O \quad (14)$$

$$Fe(OH)_2 + 2\alpha - FeOOH \rightarrow Fe_3O_4 + 2H_2O \quad (15)$$

$$H_2TiOCl_4 + 4\,OH^- \rightarrow Ti(OH)_4 + 4Cl^- + 2H_2O \quad (16)$$

$$TiOCl_2 + 4OH^- \rightarrow Ti(OH)_4 + 2Cl^- + O^{2-} \quad (17)$$

3.2. XRD and XRF Analysis. Figure 2 shows the detailed XRD analysis of the synthesized materials. As shown in Figure 2a, the XRD pattern of ilmenite sand matched with the ilmenite (ICDD no. 01-075-0519), hematite (01-073-0603), rutile (00-034-0180), and silica (01-085-0335) phases, suggesting these as the major phases with high crystallinity. The chemical composition of the ilmenite sand analyzed by XRF is tabulated in Table 1. When a sample is bombarded with X-rays, the material in the specimen emits additional X-rays. After that, a detector records the X-rays. The resulting spectrum characterizes the chemical components that make up the substance by oxide-analysis detection mode. XRF analysis revealed that ilmenite sand consisted of relatively high proportions of titanium, iron, silica, and vanadium content (48.87, 42.81, 3.94, and 1.21%, respectively) compared to the other impurities present in low quantities.

As shown in Figure 2b, the XRD pattern of the leached titanium residue matches with ICDD DB card nos. 01-076-1939, 01-083-2468, 00-041-1486, and 01-079-1095, indicating the presence of the TiO_2 (rutile), SiO_2 (quartz), $CaAl_2Si_2O_8$ (anorthite), and $AlPO_4$ (aluminum phosphate), respectively. Diffraction peaks at 27.46, 36.07, 41.20, 43.93, 54.28, 56.53, and 62.88° correspond to the (110), (101), (111), (210),

https://doi.org/10.1021/acsomega.2c03262
ACS Omega 2022, 7, 27617−27637

Table 2. Structural Properties of the Composite Analyzed by XRD Crystalline Planes

nanocomposite	component	peak position	crystalline plane	full width at half-maximum (FWHM)	integrated peak area	crystalline size (nm)	interplanar distance (nm)	percentage of component
TFTO-800	Fe_2TiO_5	25.53	(101)	0.225	178.860	37.66	0.348	71.09
	TiO_2	27.33	(110)	0.711	72.7359	11.99	0.329	28.90
TF-450	Fe_3O_4	35.71	(311)	0.816	108.006	10.67	0.252	65.74
	TiO_2	25.30	(101)	1.568	56.2736	5.42	0.351	34.25
TF-800	Fe_2O_3	33.32	(104)	0.288	133.603	30.04	0.270	56.24
	TiO_2	25.30	(101)	0.614	61.9396	13.84	0.352	26.07
	TiO_2	27.32	(110)	1.237	41.9770	6.90	0.326	17.67

(211), (220), and (002) crystalline planes of rutile.[20,52] The diffraction peak at 68.87° corresponds to the diffractions of the (031) plane of synthetic quartz.[53]

The XRD pattern of amorphous titanium is shown in Figure 2c where no clear diffractions peaks were observed. As shown in Figure 2d,e, upon calcination of amorphous titanium at 800 °C, diffraction peaks corresponding to the crystalline rutile phase of titanium dioxide (ICDD DB card no. 01-076-1939) appeared in TiO_2-A and TiO_2-B, respectively. The average crystallite size calculated from Scherrer's equation using the (110) crystalline plane for both TiO_2-A and TiO_2-B was 100.9 and 131.0 nm, respectively. The crystallite size of TiO_2 synthesized in the presence of CTAB (TiO_2-B) is higher than that of TiO_2-A, which was synthesized without CTAB. In the case without the CTAB surfactant, the $Ti(OH)_4$ chains polymerize. Polymerized chains could interact with other chains by interchain hydrogen bonding, so aggregation of TiO_2 particles and TiO_2 clusters may be formed.[54] Also, the reduction of TiO_2 cluster aggregation occurs with the presence of the CTAB surfactant in critical micelle concentration. The hydrogen atoms of the polymeric $Ti(OH)_4$ interacted with $(C_{16}H_{33})(CH_3)_3N^+$ cationic hydrophilic groups of CTAB micelles. These hydrophilic groups are removed upon calcination, resulting in less aggregated TiO_2 particles and clusters.[53]

Figure 2f shows the XRD pattern of the dried TFTO composite and diffraction pattern matched with the ICDD DB card nos. 01-077-044, 01-076-1939, and 01-073-0603, suggesting the presence of TiO_2 (anatase), TiO_2 (rutile), and α-Fe_2O_3, respectively. The diffraction peaks centered at 25.06, 35.62, 37.76, 47.23, and 62.22° can be indexed to (101), (103), (004), (200), and (211) crystalline planes of TiO_2 (anatase), respectively.[55−57] The diffraction peak at 27° is assigned to the (110) plane of TiO_2 (rutile). Similarly, the diffraction patterns centered at 32.9, 35.71, 41.12, and 62.22° correspond to the α-Fe_2O_3 (104), (110), (113), and (214) crystalline planes.[58] The diffraction peak at 54.10° can be indexed to the (105) plane of TiO_2 (anatase), (211) plane of TiO_2 (rutile), and (116) plane of α-Fe_2O_3. Figure 2g shows the XRD pattern of the 800 °C annealed TFTO-800 composite. It shows the presence of Fe_2TiO_5 (pseudobrookite) and TiO_2 (rutile), and the crystallographic data are consistent with ICDD DB card nos. 00-041-1432 and 01-076-1939, respectively. The formation of Fe_2TiO_5 phase during the annealing process required a 2:1 molar ratio of Fe/Ti. Furthermore, the absence of Fe_2O_3 and presence of TiO_2 in the XRD pattern of TFTO-800 suggested the complete conversion of Fe_2O_3 in TFTO during the phase transformation.

The XRD pattern of TFTO-800 shows prominent diffraction peaks at 18.08, 25.53, 32.50, 37.35, 40.85, 46.00, 48.87, and 60.03° corresponding to the planes (200), (101), (230), (131), (240), (331), (430), and (232) of orthorhombic pseudobrookite, Fe_2TiO_5.[20] Also, diffraction values centered with the 2θ values at 27.33, 40.85, 54.18, 56.19, and 65.60°, which corresponded to the crystalline planes (110), (111), (211), (200), (211), and (310) of rutile TiO_2.[59,60]

Figure 2h shows the XRD pattern of dried TF powder where the diffraction peaks perfectly matched with ICDD DB card nos. 01-076-1941 and 00-003-0863, suggesting the presence of TiO_2 (anatase) and Fe_3O_4 (magnetite), respectively. The diffraction peaks at 17.93, 30.30, 35.92, 43.13, 57.13, and 63.13° are assigned to the face centered cubic Fe_3O_4 (111), (220), (311), (400), (511), and (440) crystal planes, respectively.[61] The diffraction peaks of Fe_2O_3 and other impurities were not found, suggesting that only Fe_3O_4 has been formed during the synthesis during which the exact Fe^{2+} to Fe^{3+} molar ratio was maintained. The diffraction peaks at 25.20, 35.92, and 63.13° are attributed to (101), (105), and (204) crystalline planes of TiO_2 (anatase).[12] However, it was very difficult to isolate all crystalline planes of the anatase. The shielding effect of Fe_3O_4 had taken place during the precipitation.[62] Figure 2i shows the XRD pattern of the TiO_2/Fe_3O_4 nanocomposite calcined at 450 °C, which perfectly matched with ICDD DB card nos. 01-075-0033 and 00-003-0863, revealing the presence of anatase and magnetite, respectively.

The diffraction peaks at 30.12, 35.71, 43.12, 54.14, 57.32, and 63.13° are attributed to the octahedral Fe_3O_4 (220), (311), (400), (422), (511), and (440) crystalline planes.[63] This meant that the crystal structure of Fe_3O_4 has been changed from face centered cubic to octahedral upon calcination at 450 °C. Also, in Figure 2i, the diffraction peaks at 25.3, 35.71, 47.93, 54.14, 63.13, and 74.74° are indexed to the (101), (103), (200), (105), (204), and (215) crystalline planes of TiO_2 (anatase), respectively.[60] Figure 2j shows the XRD pattern of the nanocomposite calcined at 800 °C. The diffraction pattern matches with ICDD DB card nos. 01-079-1741, 01-088-1173, and 01-075-1537, indicating the presence of hematite, rutile, and anatase, respectively.[60]

The diffraction peaks at 23.91, 33.32, 35.71, 40.71, 49.53, 54.14, 57.72, 62.54, and 63.93° correspond to the (012), (104), (110), (113), (024), (116), (018), (214), and (030) diffractions of pure hematite (α-Fe_2O_3).[64,65] The compositional (changing the Fe/O ratio from 3:4 to 2:3) and structural modifications are both involved in the phase transformation from Fe_3O_4 to α-Fe_2O_3. The process is called oxygen dissociation and can occur at temperatures starting from 700 to 1000 °C, but the exact temperature varies due to composition and oxygen partial pressure. A quick hysteresis loop and back field demagnetization curve (to get coercivity and coercivity of remanence, respectively) should give a quick

https://doi.org/10.1021/acsomega.2c03262
ACS Omega 2022, 7, 27617−27637

indication of magnetite/maghemite (soft) versus hematite (hard) or a mixture of both.

Peaks at 25.30 and 27.32° are attributed to the (101) and (110) crystalline planes of anatase and rutile, respectively.[66] Table 2 summarizes the detailed analysis of Fe_2TiO_5, TiO_2 (rutile), Fe_3O_4, TiO_2 (anatase), and α-Fe_2O_3.

3.3. Raman Analysis. To confirm the crystallographic structure suggested by XRD, Raman spectroscopic analysis of synthesized materials was conducted. Figure 2 shows the Raman spectra of TFTO-800, TF-450, TF-800, and TiO_2-A materials respectively. As shown in Figure 3a, Raman analysis

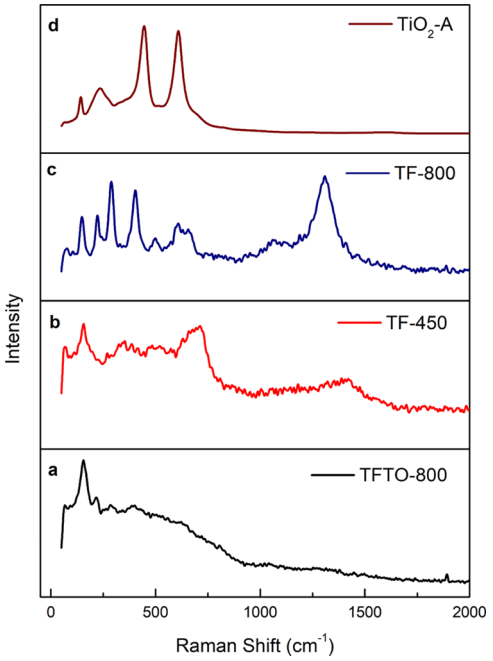

Figure 3. Raman pattern of (a) TFTO-800, (b) TF-450, (c) TF-800, and (d) TiO_2-A.

of TFTO-800 consisted of Raman vibration bands at 199, 222, 243, 290, 334, 410, 436, 610, 658, and 780 cm^{-1}. The Raman vibration bands at 199, 222, 334, 436, 658, and 780 cm^{-1} reveal the presence of the pseudobrookite (Fe_2TiO_5) phase.[20] Vibration bands at 223 and 498 cm^{-1} are the A_{1g} and the bands at 243, 290, 410, and 610 cm^{-1} are assigned to the E_g vibration modes of α-Fe_2O_3.[20,58] The observed vibration bands for α-Fe_2O_3 and Fe_2TiO_5 are consistent with the literature reported data.[20]

As shown in Figure 3b, the Raman spectra of the FT-450 nanocomposite consist of peaks located at 318, 517, and 671 cm^{-1}. Those peaks are attributed to the E_g, T_{2g}, and A_{1g} mode of Fe_3O_4.[60] To verify whether there is a phase transformation from Fe_3O_4 to γ-Fe_2O_3, the corresponding Raman spectra were intensively analyzed. These did not contain any apparent peak related to the γ-Fe_2O_3 or α-Fe_2O_3. This result gives the evidence for the existence of Fe_3O_4. The Raman band at 154 cm^{-1} is very intense and sharp. Four characteristic Raman active modes of anatase TiO_2 with symmetries E_g, B_{1g}, A_{1g}, and E_g were observed at 154, 382, 481, and 628 cm^{-1}.[67−69] These characteristic vibration frequencies confirmed the phase pure anatase TiO_2 in the TF-450 nanocomposite. An additional broad and intense Raman scattering effect was observed at 1416 cm^{-1} due to the 2LO Raman scattered intensities.[20] These Raman data confirm the formation of the pure phase of anatase and Fe_3O_4 in the TF-450 nanocomposite.

Figure 3c shows the Raman spectra of the 800 °C annealed TF-800 nanocomposite. As shown in Figure 3c, the sharp Raman vibration positions at 243 cm^{-1} were assigned to the A_{1g} and those at 290, 410, and 610 cm^{-1} were assigned to the E_g vibration modes of α-Fe_2O_3.[70,71] Similarly, the rutile TiO_2 exhibited characteristic stretching peaks at 140 and 596 cm^{-1} with relatively less intensity and correspond to the B_{1g} and A_{1g} vibration modes with respective intensity.[52] Raman vibration modes of anatase TiO_2 with symmetries E_g, B_{1g}, A_{1g}, and E_g were observed at 123, 375, 500, and 618 cm^{-1} wavenumbers with relatively less intensity.[52] These characteristic vibrational wavenumbers and their intensity ratios confirmed the presence of the α-Fe_2O_3, anatase TiO_2, and rutile TiO_2, respectively.

Figure 3d shows the 800 °C annealed TiO_2-A sample, and Raman vibration positions were centered at 142, 445, and 611 cm^{-1}, respectively. These fundamental Raman vibrations are attributed to the B_{1g}, E_g, and A_{1g} modes of rutile, accordingly.[72] A noticeable broad band at 235 cm^{-1} was observed in TiO_2-A, which did not coincide with any theoretical calculations for the fundamental Raman modes of rutile. However, the broad peak suggests that it might be either second-order or disorder induced photon scattering effect.[73]

3.4. SEM Morphological Analysis. The morphology of the synthesized nanomaterials was determined by scanning electron microscopy. The SEM image of ilmenite sand (Figure 4a) shows the macro nature of the sand particles. SEM images of synthesized TiO_2-A and TiO_2-B are shown in Figure 4b,c.

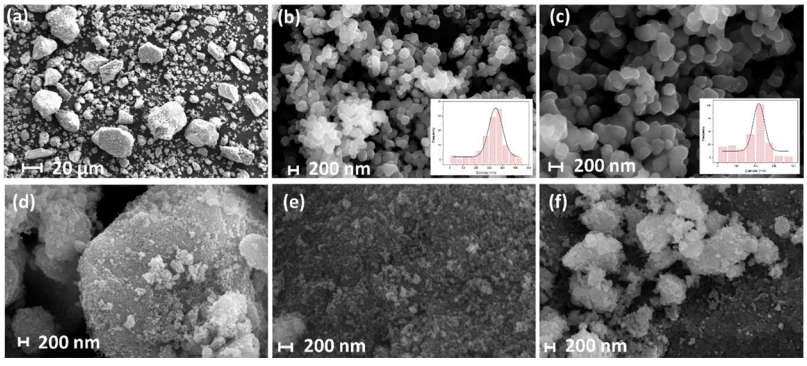

Figure 4. SEM images of the (a) ilmenite sand, (b) TiO_2-A, (c) TiO_2-B, (d) uncalcined TF composite, (e) TF-450 composite, and (f) TF-800 composite.

https://doi.org/10.1021/acsomega.2c03262
ACS Omega 2022, 7, 27617−27637

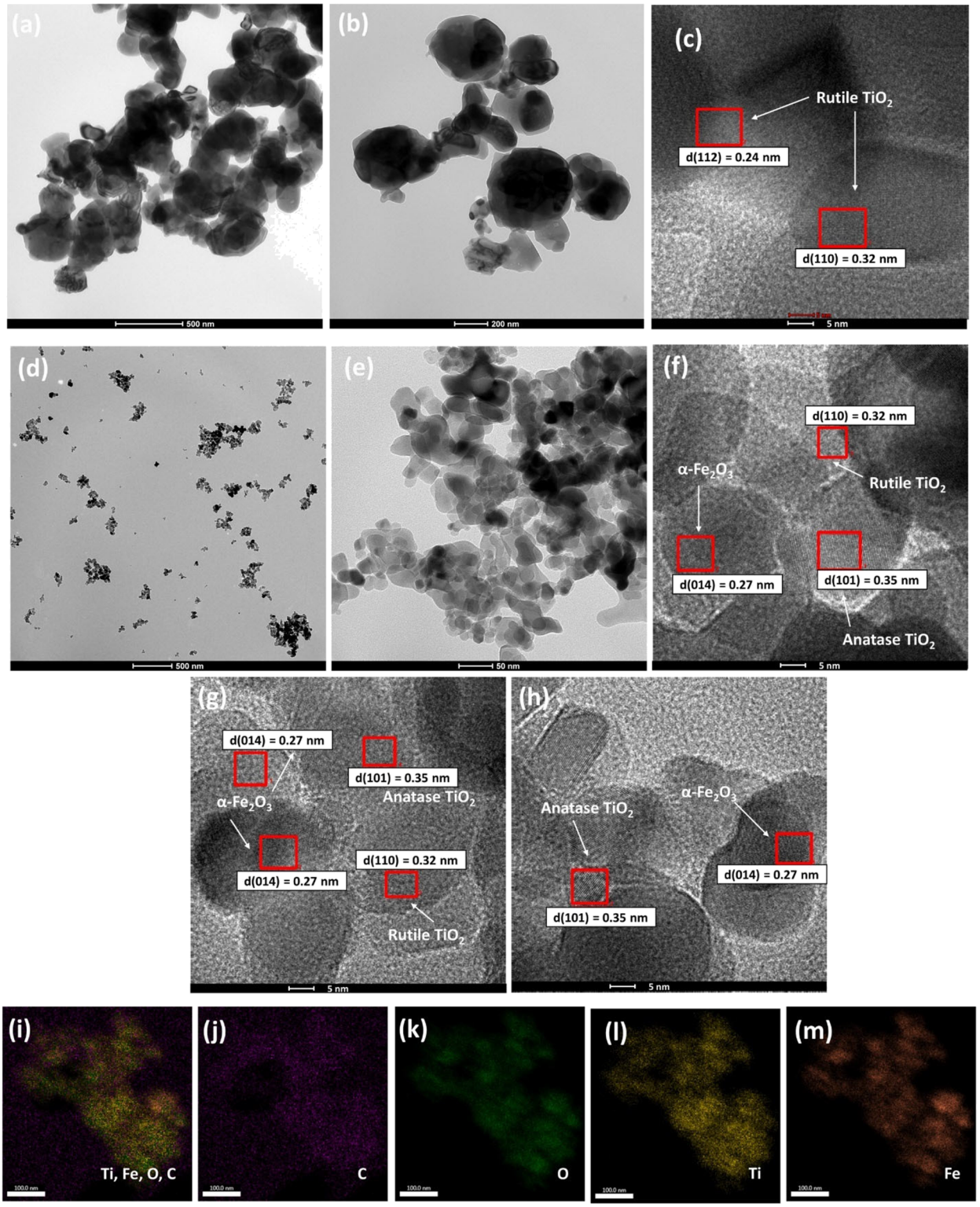

Figure 5. (a, b) Bright-field TEM images of TiO_2-A; (c) HR-TEM images of TiO_2-A; (d, e) bright-field TEM images of TF-800; (f, g, h) HR-TEM images of TF-800; (i) EDX spectra of TF-800; and elemental mapping of TF-800 (j) C, (k) O, (l) Ti, and (m) Fe.

Both TiO_2-A and TiO_2-B samples consisted of spherical nanoparticles. The average particle size of TiO_2-A and TiO_2-B was 347.2 and 218.4 nm, respectively. This result suggests that CTAB had prevented the formation of nanoparticles during the hydrothermal synthesis. The aggregation observed in the nanomaterials is due to the Oswald ripening that resulted from increased calcination temperature.[53]

3.5. TEM Analysis. The morphological features of TiO_2-A and TF-800 composites at the nanoscale were analyzed by TEM (Figure 5). Bright-field TEM images of TiO_2-A (Figure 5a,b) indicated that the nanoparticles are spherical and irregular in shape and are polydisperse with aggregated nanoparticles. The HR-TEM image of TiO_2 (Figure 5c) shows the atomic arrangement of (112) and (110) planes of

https://doi.org/10.1021/acsomega.2c03262
ACS Omega 2022, 7, 27617−27637

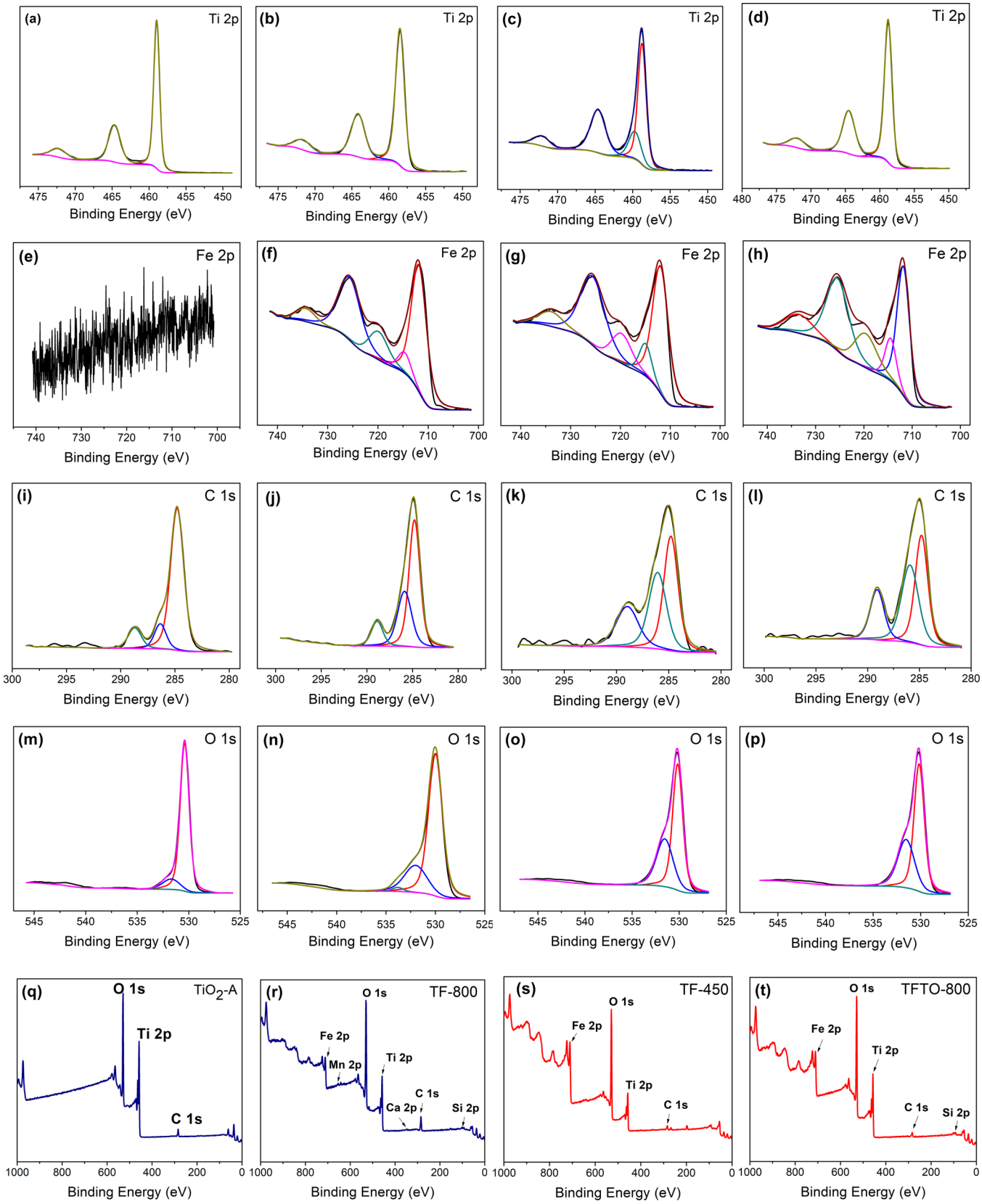

Figure 6. High-resolution XPS spectra of (a) Ti 2p of TiO_2-A, (b) Ti 2p of TF-800, (c) Ti 2p of TF-450, (d) Ti 2p of TFTO-800, (e) Fe 2p of TiO_2-A, (f) Fe 2p of TF-800, (g) Fe 2p of TF-450, (h) Fe 2p of TFTO-800, (i) C 1s of TiO_2-A, (j) C 1s of TF-800, (k) C 1s of TF-450, (l) C 1s of TFTO-800, (m) O 1s of TiO_2-A, (n) O 1s of TF-800, (o) O 1s of TF-450, and (p) O 1s of TFTO-800. Survey spectra of (q) TiO_2-A, (r) TF-800, (s) TF-450, and (t) TFTO-800.

https://doi.org/10.1021/acsomega.2c03262
ACS Omega 2022, 7, 27617−27637

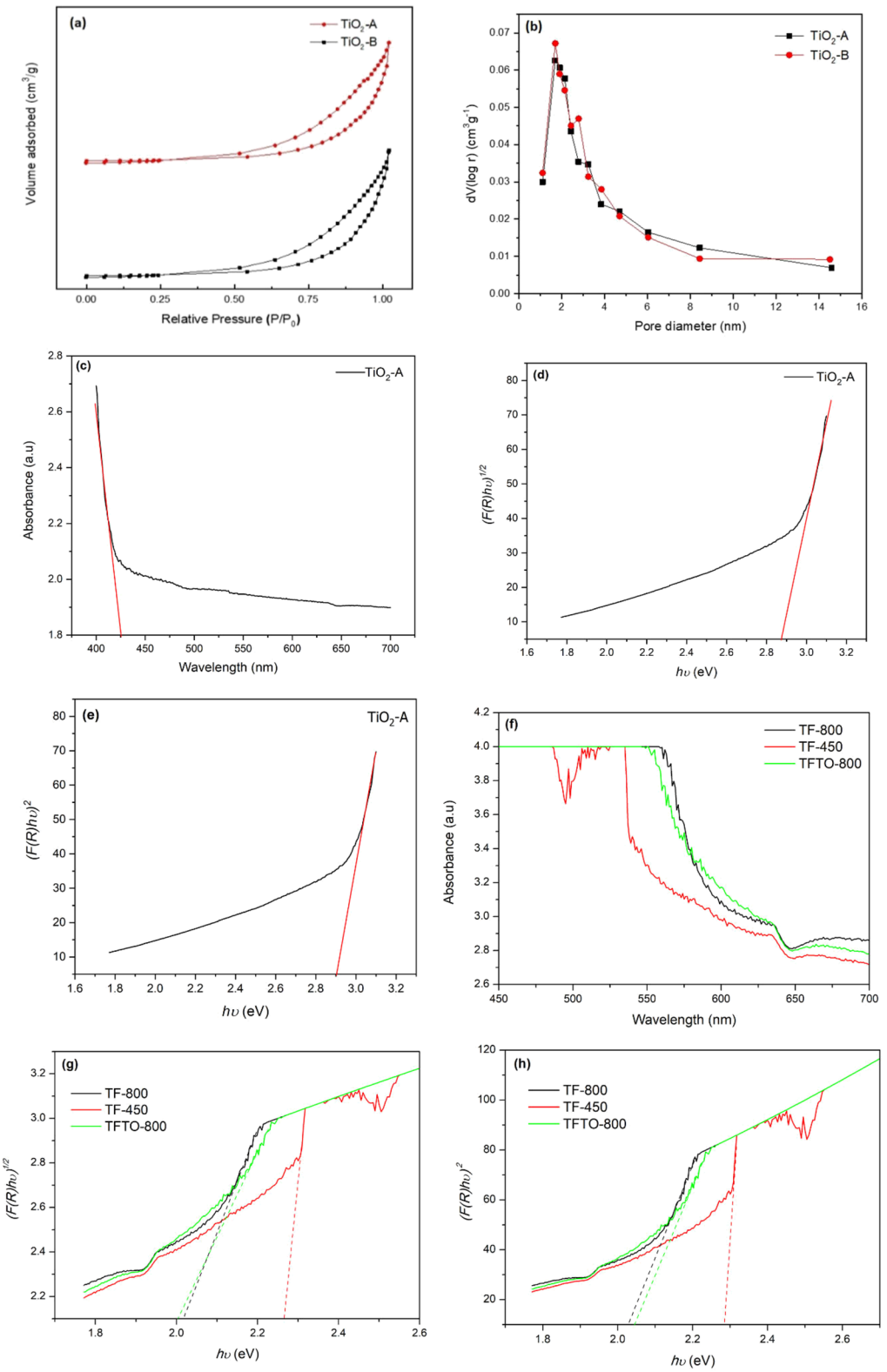

Figure 7. (a) Nitrogen adsorption−desorption isotherms of TiO_2-A and TiO_2-B; (b) pore size distribution of TiO_2-A and TiO_2-B; (c) Kubelka−Munk function vs wavelength plot for TiO_2-A; Tauc plot for determination of (d) indirect band gap (n = 1/2) and (e) direct band gap (n = 2) according to eq 19; (f) Kubelka−Munk function vs wavelength plot for TF-800, TF-450, and TFTO-800; (g) indirect band gap (n = 1/2) for TF-800, TF-450, and TFTO-800; and (h) direct band gap (n = 2) for TF-800, TF-450, and TFTO-800.

rutile, corresponding to interlayer distances of 0.24 and 0.32 nm, respectively.

Bright-field TEM images of TF-800 showed aggregated nanoparticles with spherical and irregular shapes, as shown in Figure 5d,e. Nanoparticles in TF-800 are mostly fused. Additionally, the HR-TEM image (Figure 5f−h) shows the arrangement of the atomic planes of (014) of α-Fe_2O_3, (101) of anatase, and (110) of rutile that are exhibited by interlayer

https://doi.org/10.1021/acsomega.2c03262
ACS Omega 2022, 7, 27617−27637

Table 3. Textural Properties of As-Prepared TiO_2 Samples

material	source	synthesis method	annealing temperature (°C)	surfactant	surface area S_{BET} (m^2 g^{-1})	average pore size (nm)	pore volume V_{pore} (cm^3 g^{-1})	references
TiO_2-A	ilmenite sand	hydrothermal synthesis	800		20.731	1.929	0.042	present study
TiO_2-B	ilmenite sand	hydrothermal synthesis	800	CTAB	19.419	1.541	0.037	present study
anatase TiO_2	titanium butoxide (TTB) ($Ti(OC_4H_9)_4$)	sol−gel synthesis	475	lauryl lactyl lactate	22.34	9.7	0.081	85
anatase TiO_2	TTB	reverse micelle sol−gel synthesis	500	PEG-20	71	12	0.091	86
anatase TiO_2	titanium isopropoxide (TTIP)	ultrasonic irradiation	500		38.37	10.4	0.112	87
anatase TiO_2	TTIP	solvothermal method	450		113.9	7.8	0.296	88
anatase TiO_2	TTIP	microwave method	450		116.1	9.3	0.373	88

distances 0.27, 0.35, and 0.32 nm, respectively, indicating the formation of a heterojunction between these compounds. Consequently, different exposed crystalline planes provided diverse electrochemical and catalytic properties. The (014) crystal plane of α-Fe_2O_3 nanocrystals have a higher surface energy and are more responsive to surface defects. As a result, photocatalytic activity might be affected by different exposed crystal surfaces. As shown in Figure 5i−m, images of EDX elemental maps exhibit the constituent elemental distribution of the TF-800 heterostructure. The elements Fe, Ti, and O are dispersed uniformly throughout the material. This result demonstrates the homogenous distribution of α-Fe_2O_3 and TiO_2 phases through the surface of TF-800.

3.6. XPS Analysis. X-ray photoelectron spectroscopy (XPS) was employed to study the surface composition and valence state of the synthesized materials. Figure 6 shows the high-resolution spectra of Ti 2p, Fe 2p, O 1s, and C 1s and survey spectra. High-resolution spectra of Ti 2p of TiO_2-A, TF-800, TF-450, and TFTO-800 are shown in Figure 6a,d. The high-resolution spectrum of Ti of TiO_2-A (Figure 6a) shows three peaks. Peaks at 458.97, 464.66, and 472.19 eV corresponded to the $2p_{3/2}$, $2p_{1/2}$, and satellite peak of $2p_{3/2}$ of Ti^{4+} in the TiO_2 lattice, respectively.[20,74] The satellite peak was due to a sudden change in Coulombic potential as the photo ejected electron passed through the valence band.[75] Figure 6b shows the high-resolution spectrum of Ti 2p of TF-800 with peaks at 458.48 and 464.15 eV corresponding to the $2p_{3/2}$ and $2p_{1/2}$ of Ti^{4+} in the TiO_2 lattice, respectively.[20] Figure 6c shows the high-resolution spectrum of Ti 2p of TF-450. The four peaks appeared at 458.81, 459. 68, 464.65, and 472.2 eV, which corresponded to the $2p_{3/2}$, $2p_{3/2}$, $2p_{1/2}$, and satellite peak of $2p_{3/2}$ of Ti^{4+} in the TiO_2 lattice, respectively.[20] However, the 459.68 eV binding energy corresponded to the distortion of the Ti^{4+} in the TiO_6 octahedral from TiO_2.[76] Figure 6d shows the high-resolution spectrum of Ti 2p of TFTO-800. The peaks centered at 464.49 and 458.79 eV were ascribed to Ti $2p_{3/2}$ and Ti $2p_{1/2}$, respectively, revealing that Ti elements exist mainly in the form of the Ti^{4+} oxidation state.[74]

The high-resolution spectra of Fe 2p of the synthesized materials are shown in Figure 6e−h. Figure 6e shows the high-resolution spectrum of Fe 2p of TiO_2-A, and the entire spectrum consists of noises without any sharp peaks related to the Fe $2p_{3/2}$ and Fe $2p_{1/2}$ oxidized states, revealing the absence of Fe in TiO_2-A.[53] Figure 6f shows the high-resolution spectrum of Fe 2p of TF-800. As shown in Figure 6f, the peaks of Fe 2p centered at 725.61 and 711.83 eV were attributed to $2p_{1/2}$ and $2p_{3/2}$ of Fe^{3+}, respectively.[77,78] Also, the peaks at 734.30 and 719.86 eV correspond to the satellite peaks of Fe $2p_{1/2}$ and Fe $2p_{3/2}$, indicating the oxidation state of Fe^{3+} in the TF-800.[78] The Fe 2p XPS spectrum of the TF-450 material is shown in Figure 6g. The XPS Fe 2p core-level spectra of α-Fe_2O_3, γ-Fe_2O_3, and Fe_3O_4 are known to be almost identical with each other.[77] The Fe 2p core-level spectra of TF-450 have been fitted to three main peaks at 725.57, 714.70, and 711.95 eV and two satellite peaks at 733.90 and 719.74 eV. The lowest binding energy peak at 711.95 eV was attributed to the Fe $2p_{3/2}$ of Fe^{2+}, with a corresponding satellite at 719.74 eV. The Fe $2p_{1/2}$ of Fe^{3+} tetrahedral species was found with a binding energy of 725.57 eV.[79] Iron comprised two oxidation states: Fe^{2+} and Fe^{3+} in TF-450. Figure 6h shows the XPS Fe 2p spectrum of TFTO-800. The Fe $2p_{3/2}$ and $2p_{1/2}$ main peaks are clearly accompanied with satellite structures on their high binding-energy side. The binding energy of 711.81 eV for the Fe $2p_{3/2}$ and 725.42 eV for the $2p_{1/2}$ main peaks shows the presence of Fe^{3+} in TFTO-800.[77−79] The satellite peaks were observed at 714.45, 719.6, and 733.4 eV.[20,80]

The high-resolution C 1s XPS spectra of the synthesized materials are shown in Figure 6i−l. Peaks at 284.79, 286.07, and 288.46 eV have 0.007, 0.21, and 0.100 eV standard deviation values, respectively, which are attributed to C═C, C−O, and C═O bonds, respectively.[20] Figure 6m,n shows the O 1s XPS spectra of the as-synthesized TiO_2-A, TF-800, TF-450, and TFTO-800 nanomaterials, respectively. The spectra have been fitted to two peaks with binding energies of 530.22 and 531.56 eV with standard deviations of 0.17 and 0.30 eV, respectively. The peak at 530.22 eV was ascribed to the O^{2-} of Fe^{3+}, Fe^{2+}, and Ti^{4+} oxides.[20,81] Also, the peak at around 531.5 eV of TiO_2, TF-800, and TF-450 corresponded to OH, while the peak at 532 eV of TFTO-800 corresponded to the oxygen bound to carbon.[20] The survey spectra of TiO_2-A, TF-800, TF-450, and TFTO-800 are shown in Figure 6q−t. As shown in Figure 6q, the TiO_2-A nanomaterial consisted of Ti and O as the major constituents. However, the presence of Mn, Ca, and Si in minor concentrations in other photocatalysts was observed, while Fe and Ti were the major constituents of the photocatalyst material. The Ti/Fe ratios calculated from the area under the curves of TF-800, TF-450, and TFTO-800 were 1.25, 0.29, and 3.33, respectively. Also, the C/Ti ratio calculated for TiO_2-A nanomaterial was 0.08.

3.7. Nitrogen Sorption Analysis. To distinguish the effect of the CTAB surfactant for the formation of a porous structure, TiO_2 samples were subjected to Brunauer−

https://doi.org/10.1021/acsomega.2c03262
ACS Omega 2022, 7, 27617−27637

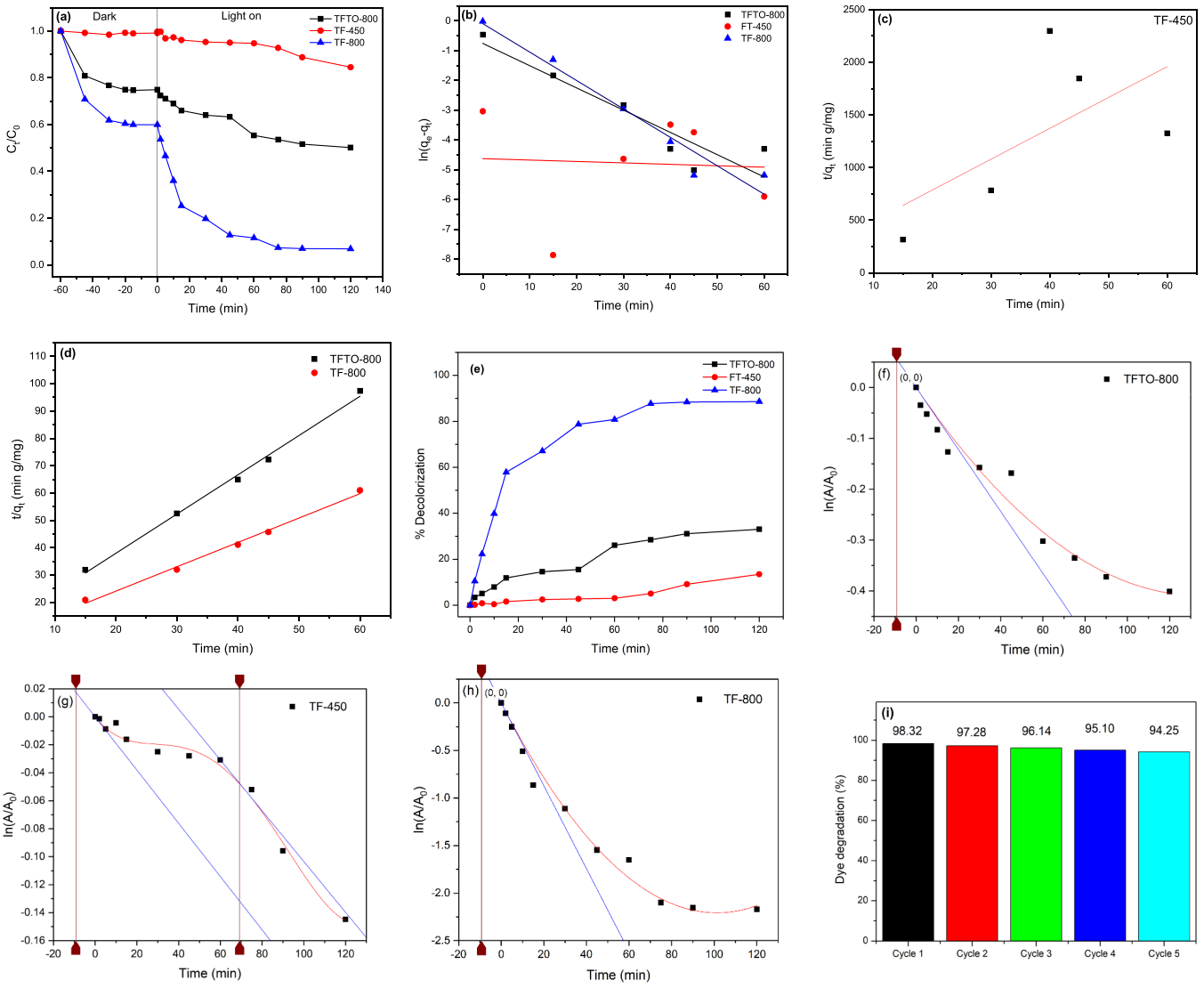

Figure 8. (a) Degradation rate of MB at the different time intervals; (b) pseudo-first-order model of TFTO-800, TF-450, and TF-800; (c) pseudo-second-order model of TF-450; (d) pseudo-second-order model of TFTO-800 and TF-800, dark 60 min adsorption of MB onto the prepared nanocomposite; (e) photocatalytic % decolorization of MB; first-order kinetic photodegradation of MB under LED light for (f) TFTO-800, (g) TF-450, and (h) TF-800 nanocomposites; and (i) conversion of MB at each photocatalytic cycle of TF-800.

Emmett−Teller (BET) analysis to acquire nitrogen sorption isotherms and the BJH pore size distribution curves that are shown in Figures 7a and 6b, respectively. Nitrogen sorption isotherms of both TiO_2-A and TiO_2-B samples exhibit a type (III) isotherm, and it did not show any hysteresis loop.[82−84] This isotherm referred to a nonporous or macroporous (>50 nm) material that was obtained due to the relatively week interactions between the adsorbent and adsorbate (TiO_2 and N_2 molecules). The BJH pore size distribution curves of both TiO_2 materials show identical behavior with uniform pore distribution. The specific surface area, pore volume, and average pore diameters for prepared TiO_2-A and TiO_2-B samples are tabulated in Table 3. It was found that the BET surface area and pore volume were similar for TiO_2-A and TiO_2-B. These results were attributed to the similar formation conditions of TiO_2 either with CTAB or without CTAB. In the case of hydrothermal synthesis, the structures of CTAB micelles are less stable under 180 °C. This instability of CTAB micelles resulted to the noncontrollable polymerization of $Ti(OH)_4$ in TiO_2-B. Further, as reported in the literature, the titanium source, synthesis method, annealing temperature, and type of the surfactant used significantly contributed to the surface area, pore size, and pore volume of the synthesized TiO_2 nanoparticles as shown in Table 3.

3.8. Optical Adsorption Properties. The UV−vis DRS optical absorption properties of the prepared TiO_2-A are shown in Figure 7c−e. In Figure 7c, the Kubelka−Munk function was plotted against wavelength. The TiO_2-A solid reveals an abrupt drop of absorption at about 400 nm, indicating an increase in radiation absorption below this wavelength. Also, it can be seen that TiO_2 exhibits a typical high absorption in the UV region and almost no absorption in the visible region. The adsorption edge for TiO_2-A was approximately 425 nm. This event is associated with the electron transition from the valence band to the conduction band in the rutile structure. On the other hand, diffuse reflectance UV−vis data were used to calculate the band gap energy. The band gap energy was calculated from the plot of $[F(R)h\nu]^n$ vs $h\nu$ (photon energy). The value of n used for the direct and indirect allowed transitions is 2 and $^1/_2$, respectively.

https://doi.org/10.1021/acsomega.2c03262
ACS Omega 2022, 7, 27617−27637

Table 4. Kinetic Parameters for Dark Adsorption of Methylene Blue onto Nanocomposites

		pseudo-first-order model			pseudo-second-order model		
material	$q_{e,\,exp}$ (mg g^{-1})	q_e (mg g^{-1})	k_1 (min^{-1})	r_1^2	q_e (mg g^{-1})	k_2 (g mg^{-1} min^{-1})	r_2^2
TFTO-800	0.690		0.075	0.826	0.696	0.224	0.994
TF-450	0.048		0.005	0.246	0.034	4.347	0.180
TF-800	1.090		0.095	0.938	1.123	0.126	0.992

The Kubelka–Munk function, $F(R)$, is given by eq 18, and the band gap was determined using to the Tauc plot.[89]

$$F(R) = \frac{\alpha}{S} = \frac{(1-R)^2}{2R} \tag{18}$$

$$[F(R)h\nu]^n = A(h\nu - E_g) \tag{19}$$

where α = absorption coefficient (a.u), S = dispersion factor, R = diffuse reflectance of the sample divided by the reflectance of the reference material ($BaSO_4$), h = Planck's constant (4.1357×10^{-15} eV s), E_g = band gap (eV), and A = proportional constant.

According to Figure 7d,e, the calculated direct and indirect band gap energies for the synthesized TiO_2-A are 2.91 and 2.88 eV, respectively. The band gap that resulted from the direct transition was chosen, and it was lesser than the theoretical band gap value reported for rutile (3.0 eV).[90] According to the XRF analysis, vanadium (V) is present at a weight percentage of 1.22%. Vanadium easily gets doped to the TiO_2 lattice as the ionic radius of vanadium is quite similar to that of titanium and thus lowers the band gap of rutile by creating an energy level below the conduction band of TiO_2.[56,91] However, according to the XRD, Raman, and XPS analysis of TiO_2-A and TiO_2-B, the crystalline parameters related to the standard rutile TiO_2 are precisely equivalent to those in the TiO_2 in TiO_2-A and TiO_2-B. These results suggested that V doped into the TiO_2 lattices and it may not deposit on the surface of TiO_2 as heterostructures.

Furthermore, Figure 7f shows the Kubelka–Munk function plotted against the wavelength of TF-800, TF-450, and TFTO-800. As shown in Figure 7f, TF-800 and TFTO-800 reveal an abrupt drop of absorption at the visible light region. However, TF-450 shows an adsorption edge far away from the TF-800 and TFTO-800 photocatalysts. The direct and indirect band gap responsible for the TF-800 and TFTO-800 is illustrated in Figure 7g,h, respectively. The indirect band gap for TF-800, TF-450, and TFTO-800 can be assigned as 2.01, 2.00, and 2.26 eV, respectively. In addition to that, the direct band gap for the direct transcription of TF-800, TF-450, and TFTO-800 can be assigned as 2.02, 2.04, and 2.28 eV, respectively.

3.9. Photocatalytic Degradation. The photocatalytic activities of the prepared TFTO-800, TF-450, and TF-800 samples were evaluated based on degradation of 10 mg/L methylene blue dye (MB) under visible light irradiation (Figure 8). The experiments were performed under the following conditions: C_0 = 10 mg/L, T = 25 °C, and pH = 7. C_t is the absorbance at different time intervals, and C_0 is the initial MB concentration.

The photodegradation of MB under visible light is shown in Figure 8a. Catalysts were shaken with the MB solution under dark conditions for 60 min until adsorption–desorption was reached as shown in Figure 8a.

TF-450 did not show a significant capacity to adsorb MB. However, TFTO-800 and TF-800 did adsorb MB, where a significant adsorption was observed during the first 15 min because, initially, the surface of all the catalysts was vacant. With time, the progress rate of adsorption decreased, reaching an adsorption–desorption equilibrium at 60 min. As adsorption sites became occupied, available vacant sites for MB molecules became limited, resulting in low adsorption. Moreover, though adsorption sites may be available, incoming molecules cannot reach those sites due to the high steric hindrance of the preadsorbed MB molecules.[92,93] To study the adsorption kinetics, data obtained under dark conditions were fitted to pseudo-first-order and pseudo-second-order kinetics models. The best fitting model was selected based on the linear regression correlation coefficient (r^2) values. A linear form of the pseudo-first-order and pseudo-second-order adsorption models could be expressed by eqs 20 and 21.[94] The plot for the pseudo-first-order kinetics model for all three catalysts is shown in Figure 8b. The plot that represents the pseudo-second-order kinetic model of TF-450 is given in Figure 8c, and that of TFTO-800 and TF-800 is shown in Figure 8d. Corresponding kinetic parameters are summarized in Table 4. The reusability of the TF-800 photocatalyst was evaluated for 3 h to determine how effective the catalysts would be when used multiple times. The initial concentration and volume of MB were 10 mg/L and 100 mL, respectively. The efficiency of TF-800 in photodegrading MB under visible light dropped from 98.32% at the first cycle to 94.25% at the fifth cycle, as illustrated in Figure 8i. There was only a 4.07% decrease in conversion of MB from cycle 1 to cycle 5, which may have been caused by an accumulation of MB molecules in the porous structure that slows the movement of fresh MB molecules to the catalytically active sites.

$$\ln(q_e - q_t) = \ln q_e - k_1 t \tag{20}$$

$$\frac{t}{q_t} = \frac{1}{k_2 q_e^{\,2}} + \left(\frac{1}{q_e}\right)t \tag{21}$$

where q_e = amount of adsorbed (adsorbate) at equilibrium per unit mass of adsorbent (mg/g), q_t = amount of adsorbed (adsorbate) at time t per unit mass of adsorbent (mg/g), k_1 = pseudo-first-order adsorption rate constant (1/min), t = time (min), and k_2 = pseudo-second-order adsorption rate constant (g/min * mg).

The adsorption data of TFTO-800 and TF-800 fitted well with the pseudo-second-order model with a linear regression correlation coefficient of 0.99. Also, as shown in Table 4, the experimental equilibrium adsorption capacity ($q_{e,\,exp}$) of TFTO-800 and TF-800 is well aligned with the theoretical equilibrium adsorption capacities calculated from the pseudo-second-order model. Furthermore, the k_2 value of TFTO-800 was higher than the k_2 value of TF-800, indicating that the rate of adsorption of MB onto TFTO-800 is greater than TF-800, which could be due to the high surface area and pore volume.

The photocatalytic activity of the synthesized catalysts was evaluated based on the degradation of MB upon exposure to visible light. The photodegradation efficiency of the catalysts is

https://doi.org/10.1021/acsomega.2c03262
ACS Omega 2022, 7, 27617−27637

shown in Figure 8e. The percentage decolorization was calculated by eq 22. The maximum percentage decolorization (88.6%) occurred when TF-800 was used as the photocatalyst followed by TFT0-800 (33.1%) and TF-450 (13.5%). The efficient photodegradation removal percentage of TF-800 due to the maximization of charge separation through the heterostructure explained in Section3.9.

$$\%\text{Decolorization} = \left(\frac{A_0 - A}{A_0}\right) \times 100 \tag{22}$$

where A_0 = absorbance of MB at zero time and A = absorbance of MB at time t.

Photocatalytic degradation kinetics of organic molecules usually follows the Langmuir−Hinshelwood kinetics mechanism, and the simplified equation can be expressed as in eq 23.[95,96]

$$\ln\left(\frac{C}{C_0}\right) = -kKt = -K_{app}t \tag{23}$$

where C = concentration of MB at time t (mg/L), C_0 = initial concentration of MB (mg/L), k = reaction rate constant (1/min), K = adsorption coefficient of the reactant, K_{app} = apparent first-order rate constant (1/min), and t = time (min).

Figure 8f−h shows the first-order kinetic data points ($\ln(A/A_0)$, t) fit to a polynomial order function equation. The polynomial equations obtained for TFTO-800, TF-450, and TF-800 are represented in eqs 24, 25, and 26, respectively. The data points ($\ln(A/A_0)$, t) obtained for TF-800 and TFTO-800 nanocomposites fitted well to the second-order polynomial regression, while those obtained for TF-450 fitted well to the fourth-order polynomial regression. The correlation coefficient (r^2) indicates how well the data fitted to the respective equations. The r^2 values and rate constants for TFTO-800, TF-450, and TF-800 photocatalysts for both linear and polynomial functions are tabulated in Table 5.

$$y = 2.26 \times 10^{-5}x^2 - 6.09 \times 10^{-3}x \tag{24}$$

$$y = 4.28 \times 10^{-9}x^4 - 1.04 \times 10^{-6}x^3 + 6.92 \times 10^{-5}x^2 - 1.91 \times 10^{-3}x \tag{25}$$

$$y = 2.15 \times 10^{-4}x^2 - 0.04x \tag{26}$$

where $y = \left(\ln\left(\frac{A}{A_0}\right)\right)$ and x = exposure time $(t)/(\text{min})$.

Table 5 shows that the initial rate constant for the photodegradation of MB in the presence of TF-800 (0.044 min^{-1}) was higher than that of TFT0-800 (0.006 min^{-1}) and TF-450 (0.002 min^{-1}). When the catalysts are illuminated by photons with energy higher than the band gap energy, photo-generated electrons are excited from the valence band (VB) to the conduction band (CB), leaving holes in the VB. When the surface of TFTO-800, TF-450, and TF-800 photocatalysts is illuminated by visible light, TiO_2 is not expected to show a significant contribution to the photocatalytic activity because the energy of the incoming photons is insufficient to promote an electron from the VB to the CB. However, in the presence of only visible light, TiO_2 merely serves as an electron transport layer.[97] The electron transport layer can selectively collect photogenerated charge carriers produced in the visible light sensing absorber material and limit the recombination of carriers at interfaces, thus ensuring a high photocatalytic efficiency. Synthesized nanocomposites consisted of a visible light active component Fe_2TiO_5, Fe_3O_4, and α-Fe_2O_3 in TFTO-800, TF-450, and TF-800, respectively. The theoretical band gap of spinel cubic Fe_3O_4 is 0.14 eV, that of Fe_2TiO_5 is around 2.25 eV, and that of α-Fe_2O_3 is 2.1 eV, respectively.[98−100] Those visible-light active materials can promote the initial excitation of electrons from the CB to the VB. The band alignment of the individual component in the nanocomposite is very important for the photocatalytic activity.

Table 5. Linear and Polynomial Kinetic Parameters for Visible Light Photocatalysis

	linear regression analysis		polynomial regression analysis	
material	K_{app} (min^{-1})	r_L^2	initial rate constant (min^{-1})	r_P^2
TFTO-800	0.004	0.960	0.006	0.985
TF-450	0.001	0.927	0.002	0.990
TF-800	0.024	0.929	0.044	0.993
P-25	0.0001	0.973		

The TF-450 nanocomposite exhibited the lowest photoactivity. As revealed by the XRD analysis, TF-450 consisted of approximately 65.7% of Fe_3O_4 and 34.2% of TiO_2. This decrease in photocatalytic activity could have occurred because of the photo-dissolution of iron oxide induced by photoactive TiO_2 due to electronic interactions at the phase junction.[101,102] As confirmed by the XRD analysis, Fe_3O_4 has a spinel cubic structure that has a band gap of 0.14 eV.[98,103−105] Hence, the Fe_3O_4/TiO_2 phase junction exhibits a relatively large difference in energy gap between n-type semiconductors of rutile TiO_2 (3.2 eV) and Fe_3O_4 (0.14 eV). Photo-generated electrons in the excited Fe_3O_4 cannot transfer to the CB of TiO_2. The calculated CB and VB energy for Fe_3O_4 is 1.21 and 1.35 eV, respectively. Therefore, the narrow band gap of Fe_3O_4 enhances the recombination of electron−hole pairs, resulting in low photocatalytic activity in TF-450. The initial photocatalytic rate constant of TFTO-800 was 3 times faster than TF-450.

The TFTO-800 binary nanocomposite consisted of 71.1% Fe_2TiO_5 and 28.9% TiO_2. Fe_2TiO_5 facilitated the initial excitation of electrons from CB to VB in the TFTO-800 binary nanocomposite. As reported in our previous study, Fe_2TiO_5/TiO_2 shows a type I band alignment.[74] Therefore, as the CB of TiO_2 lies above the CB of Fe_2TiO_5, migration of photogenerated electrons from Fe_2TiO_5 to TiO_2 would not take place. Hence, electron−hole pair recombination is possible at Fe_2TiO_5. Therefore, the photocatalytic activity of TFTO-800 is greater than TF-450 but less than TF-800. The initial rate constant for the photodegradation of MB in the presence of TF-800 was 6 times higher than TFTO-800 and 22 times faster than TF-450.

The TF-800 nanocomposite consisted of 56% α-Fe_2O_3, 26% anatase TiO_2, and 17% rutile TiO_2. The band gap energy of rutile and anatase polymorphs of TiO_2 is at 3.03 and 3.2 eV, respectively. The CB of anatase lies 0.17 eV above that of rutile TiO_2. This type of band alignment could facilitate an excellent transfer of electrons from anatase to rutile, producing a higher photocatalytic activity. As shown in Figure 9a, upon expose to the visible light irradiation, excited electrons in α-Fe_2O_3 transferred to the CB of anatase and followed by CB of rutile and the reduction of O_2 taken place at the CB of rutile. On the

https://doi.org/10.1021/acsomega.2c03262
ACS Omega 2022, 7, 27617−27637

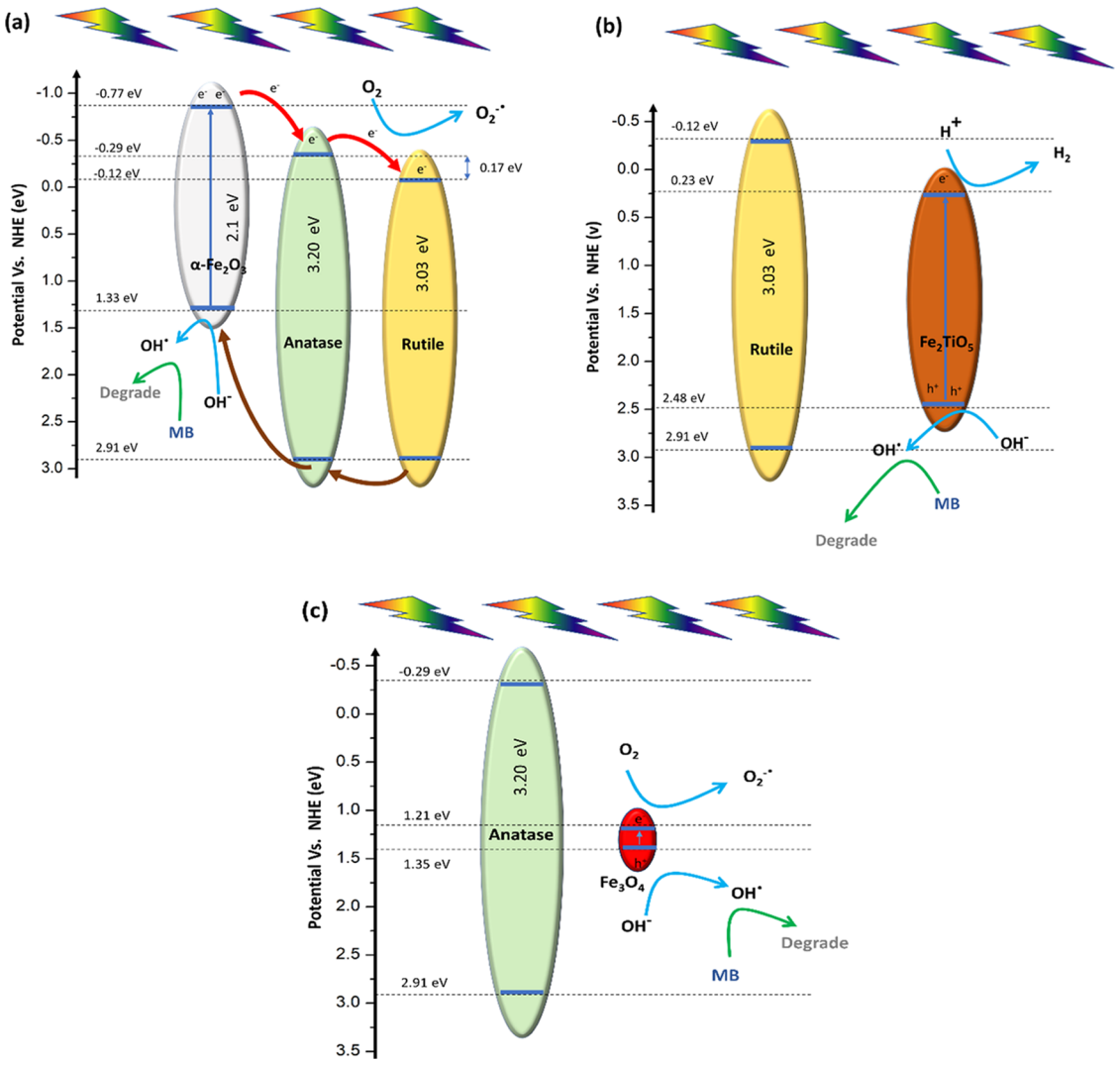

Figure 9. Schematic illustration of the possible charge separation band alignment structure of (a) TF-800, (b) TFTO-800, and (c) TF-450.

other hand, holes are initially exhibited at the VB of anatase and rutile due to the overlapping of VB energy levels. Furthermore, holes are migrated to the VB of α-Fe_2O_3 from the VB of anatase and rutile. This type of band alignment of TF-800 is type II where the photo-generated electrons of Fe_2O_3 migrate to the CB of TiO_2, facilitating the charge separation and leading to higher photocatalytic activity by limiting the electron−hole recombination effects. According to these results, it is evident that the ternary TF-800 nanocomposite is more effective than binary TF-450 and TFTO-800 nanocomposites in photodegrading MB under visible light exposure. Similarly, the visible light-driven photocatalytic decomposition of MB in the presence of P-25 was examined. First-order deterioration is depicted in Figure S1. The linear first-order rate constant calculated for P-25 was 0.0001 min^{-1}. The photocatalytic decomposition of MB in the presence of TF-800, TFTO-800, and TF-450 catalysts was 440, 60, and 20 times faster than that of P-25, respectively.

There is a lack of research work to evaluate kinetic parameters of dye degradation by photocatalyst materials synthesized from ilmenite sand. However, the photocatalytic performance of the TF-800 nanocomposite for MB degradation was compared with the first-order degradation rate of other ilmenite sand-based photocatalyst materials (Table 6). Based on the information available, TF-800 showed higher initial degradation rate compared to the other materials.

3.10. Determination of Band Alignment in Photocatalysts. The mechanism of charge separation and the band

Table 6. First-Order Degradation Rates of Organic Dye by Ilmenite Sand Based Photocatalysts

material	irradiation source	pollutant	rate (min^{-1})	reference
$TiO_2/TiO_2/Fe_2O_3$	LED	MB	0.044	present work
$Fe_2TiO_5/Fe_2O_3/TiO_2$	LED	MB	0.011	20
Fe_2TiO_5/TiO_2	solar energy	MB	0.008	74
ilmenite	solar energy	Reactive Black 5	0.040	106
TiO_2/α-Fe_2O_3	UV light	indigo carmine	not clearly specified	107
pretreated ilmenite sand	visible light	Reactive Black 5	0.018	108
pretreated ilmenite	visible light	MB	0.023	109
TiO_2 synthesized from ilmenite	UV light	Rhodamine B	0.002	90

https://doi.org/10.1021/acsomega.2c03262
ACS Omega 2022, 7, 27617−27637

alignment of TF-800, TFTO-800, and TF-450 are schematically illustrated in Figure 9. The band gap values determined from diffuse reflectance spectroscopic analysis for anatase TiO_2, rutile TiO_2, α-Fe_2O_3, Fe_2TiO_5, and Fe_3O_4 are 3.20, 3.03, 2.0, 2.25, and 0.14 eV, respectively. Potentials of the conduction band and the valance band were calculated by formulas 27 and 28, respectively.

$$E_{CB} = X - E^c - 0.5\,E_g \quad (27)$$

$$E_{VB} = X - E^c + 0.5\,E_g \quad (28)$$

where X = absolute electronegativity of the semiconductor, which is defined as the geometric mean of the absolute electronegativity of the constituent atoms; E^C = energy of free electrons on the hydrogen scale; E_g = band gap of the semiconductor; E_{CB} = conduction band (CB) position; and E_{VB} = valance band (VB) position.

The absolute electronegativity values for anatase-TiO_2, rutile-TiO_2, and α-Fe_2O_3 are 5.81, 5.81, and 4.76 eV, respectively.[20] Also, the energy of free electrons on the hydrogen scale is 4.5 eV vs NHE. The parameters toward the calculation of VB and CB energy position have been tabulated in Table 7.

Table 7. Parameters behind the Calculation of VB and CB Energy

semiconductor oxide	electronegativity (X)	E_g (eV)	calculated CB position (eV) (NHE)	calculated VB position (eV) (NHE)
anatase TiO_2	5.81	3.20	−0.29	2.91
rutile TiO_2	5.89	3.03	−0.12	2.91
α-Fe_2O_3	4.78	2.10	−0.77	1.33
Fe_2TiO_5	4.78	2.25	0.23	2.48
Fe_3O_4	5.78	0.14	1.21	1.35

XPS data were further analyzed to provide additional evidence for the electron transfer mechanism of the synthesized TF-800 composite. The binding energy of Fe $2p_{3/2}$ of pure α-Fe_2O_3 is reported to be at 709.32 eV.[20] The binding energy of Fe $2p_{3/2}$ in TF-800 appeared at 711.95 eV, suggesting a decrease in the electron concentration at α-Fe_2O_3 of TF-800.[112] The degree of delocalization and/or electronic coupling between TiO_2 empty electronic states can be demonstrated by proving that α-Fe_2O_3 impacts electronic states around the Fermi level.[113] As a result of the low electron density at iron-based species, photogenerated electrons are readily taken up by TiO_2, resulting in the production of $^{\bullet}O_2^-$, which degrades MB as proposed by the mechanism. The binding energy of Ti $2p_{3/2}$ in pure TiO_2 is reported to be at 459.36 eV,[20] while Ti $2p_{3/2}$ of TF-800 appeared at 458.48 eV, indicating a 0.88 eV decrease in binding energy and suggesting that TiO_2 is enriched with electrons. Therefore, it is evident that there is a net electron flow from Fe_2O_3 to TiO_2 in TF-800. As a result, $O_2^{\bullet-}$ radicals are formed at the CB band of TiO_2, while $^{\bullet}OH$ radicals are generated at the VB band of Fe_2O_3.[114]

3.11. Sacrificial Agent Study of TF-800. Radical scavenging tests were carried out to determine the primary active radical species for the degradation of MB in the presence of TF-800. In summary, EDTA, IPA, and PS were introduced to the degrading system to determine the effect of h^+, $^{\bullet}OH$, and $^{\bullet}S_2O_8^-$, respectively.[110] All the parameters were kept constant where 8 mmol of the above reagents was added just before switching on the light. Readings were collected for 2 h under illumination. Figure 10a shows the reduction of the MB concentration with time. The PS added system showed a rapid reduction in the MB concentration where the concentration reached zero in 30 min. Figure 10b exhibits the first-order kinetics, while the rate constants calculated are expressed in Figure 10c. No sacrificial agent or PS was used in the control experiment. Table 8 summarizes the rate constants and the R^2 values. Linear first-order degradation rate constants for the systems with MB and TF-800 only and for the systems with IPA, EDTA, and PS additionally were 0.023, 0.007, 0.008, and 0.079 min^{-1}, respectively. The PS system was 3.43 times faster than the system with MB and TF-800 only, which acted as the control.

As shown in Figure 10d, the concentration of MB after the degradation process in which EDTA, IPA, and PS were used was 2.82, 2.97, and 0.11 mg/L, respectively, and the calculated removal efficiency for EDTA, IPA, and PS was 72.67, 71.22, and 99.12%, respectively, while that in the control experiment was 93.02%. There was no difference in the photocatalytic degradation of MB when EDTA and IPA were introduced, indicating that the effect of adding both reagents is the same.

Several tests were carried out to investigate the active species involved in the MB degradation process of TF-800. Generally, IPA is considered as an excellent $^{\bullet}OH$ scavenger, while EDTA is a h^+ scavenger.[111] IPA and EDTA substantially inhibited the ultimate breakdown efficiency of MB as shown in Figure 10 almost equally, suggesting that both $^{\bullet}OH$ and h^+ are responsible for the degradation of MB. Further, $^{\bullet}OH$ is generated by the action of h^+. Therefore, when h^+ is scavenged automatically, the $^{\bullet}OH$ concentration also declines, further reducing the MB degradation. PS accelerated the visible light driven photocatalysis by yielding $SO_4^{\bullet-}$ radicals according to eqs 29−31. Further, $S_2O_8^{\bullet-}$, the source of $SO_4^{\bullet-}$, is also generated when OH^- is present in the medium, further increasing the rate of the reaction.

$$TF - 800 + \text{visible light} \rightarrow e^- + h^+ \quad (29)$$

$$S_2O_8^{2-} + h^+ \rightarrow S_2O_8^{\bullet-} \quad (30)$$

$$S_2O_8^{2-} + e^- \rightarrow {}^{\bullet}SO_4^- + SO_4^{2-} \quad (31)$$

$$SO_4^{\bullet-} + OH^- \rightarrow SO_4^{2-} + {}^{\bullet}OH \quad (32)$$

$$SO_4^{\bullet-} + S_2O_8^{2-} \rightarrow SO_4^{2-} + S_2O_8^{\bullet-} \quad (33)$$

4. CONCLUSIONS

Highly pure TiO_2 spheres were successfully synthesized using natural ilmenite sand as the raw material via a combination of acid digestion and hydrothermal synthesis pathways. Synthesized TiO_2 spheres passivated with CTAB possess a higher pore volume and contain more than 98.5% TiO_2, with vanadium being the only impurity. The band gap that resulted from the direct transition of TiO_2 is 2.91 eV, which is less than that of rutile (3.0 eV) due to the presence of V, which has doped to TiO_2, lowering the band gap. The corrosive and ecologically harmful acid leachate produced during the leaching of ilmenite sand was successfully converted into highly efficient visible light active photocatalysts, such as TFTO-800, TF-450, and TF-800. Among them, TF-800 nanocomposite was very efficient and showed the highest rate for the photodegradation of methylene blue (0.044

https://doi.org/10.1021/acsomega.2c03262
ACS Omega 2022, 7, 27617−27637

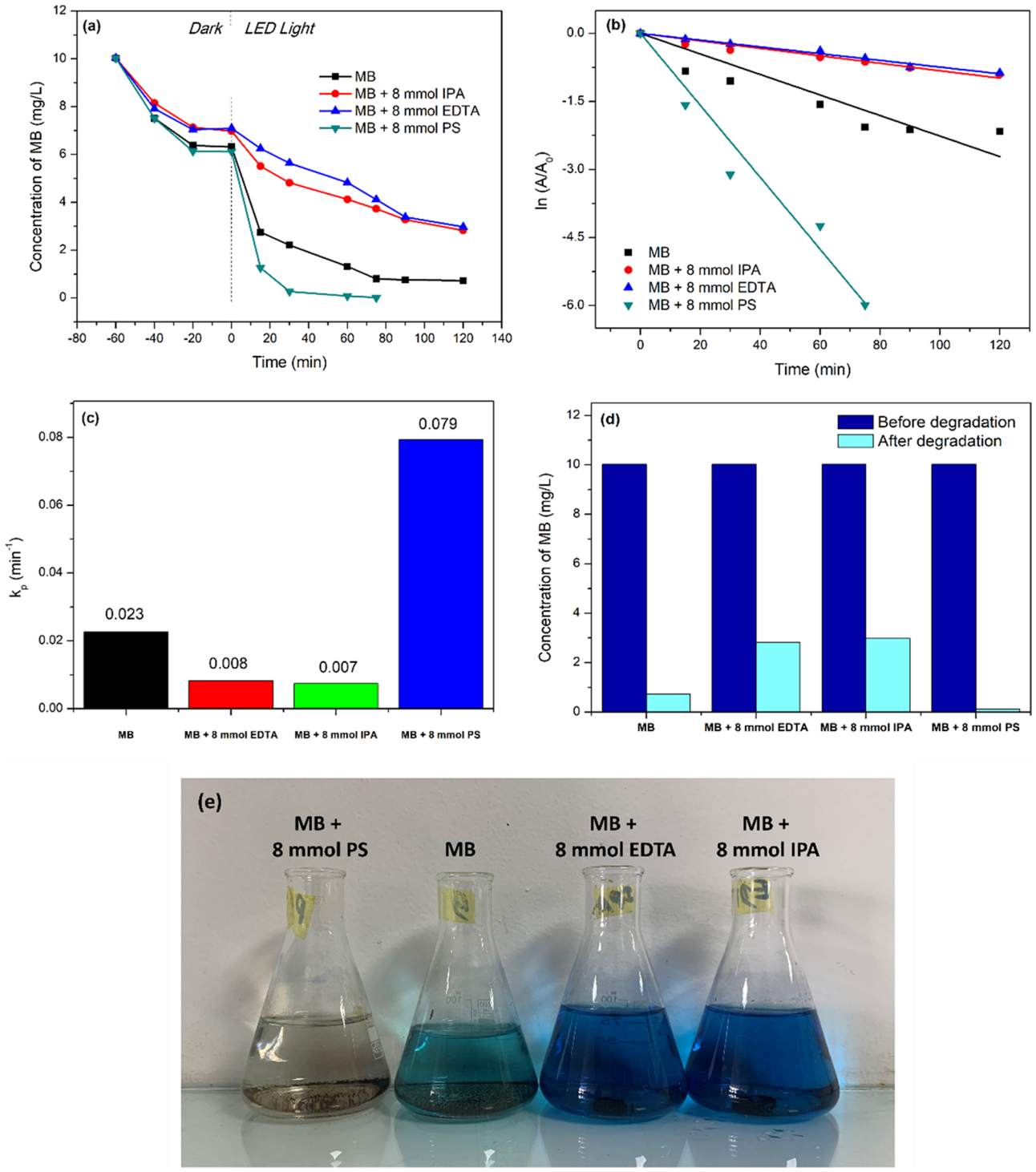

Figure 10. (a) Comparative degradation of the MB concentration with scavengers by the TF-800 heterostructure at the different time intervals, (b) first-order kinetic degradation of MB by the TF-800 heterostructure, (c) histogram of first-order photodegradation rate constants for the TF-800 heterostructure with scavengers, (d) concentration of MB in the photocatalyst system before and after the degradation, and (e) photodegraded reaction system after 75 min.

Table 8. Kinetic Parameter Evaluation for MB Degradation

agent	concentration of sacrificial agent (mmol)	degradation rate (min^{-1})	r^2
		0.023	0.942
IPA	8	0.007	0.981
EDTA	8	0.008	0.993
PS	8	0.079	0.981

min^{-1}), while rate constants of TFTO-800 and TF-450 are 0.006 and 0.002 min^{-1}, respectively. The TF-800 nanocomposites absorb visible light due to the presence of α-Fe_2O_3, and anatase-TiO_2 and rutile-TiO_2 band alignment promotes excellent charge separation throughout the heterojunction. The synthesized TF-800 ternary nanocomposite showed pseudo-second-order kinetics for the adsorption of MB in the dark with a rate of 0.126 g mg^{-1} min^{-1}, revealing the chemisorption

https://doi.org/10.1021/acsomega.2c03262
ACS Omega 2022, 7, 27617−27637

of MB to the adsorbent. XRD and Raman analysis confirmed the crystal nature of the synthesized nanomaterials. The XRD analysis of the TF-800 nanocomposite confirmed heterostructure composed by 56.24, 26.07, and 17.67% of α-Fe_2O_3, anatase TiO_2 and rutile TiO_2, respectively. XPS data revealed that the surface of TF-800 is composed of Fe^{3+} and Ti^{4+} oxidation states. The initial photodegradation rate was the highest value reported in the literature for the ilmenite sand based photocatalysts.

■ ASSOCIATED CONTENT

Supporting Information

The Supporting Information is available free of charge at https://pubs.acs.org/doi/10.1021/acsomega.2c03262.

Visible light driven first-order degradation rate of P-25 (PDF)

■ AUTHOR INFORMATION

Corresponding Authors

Charitha Thambiliyagodage − *Faculty of Humanities and Sciences, Sri Lanka Institute of Information Technology, Colombo 10115, Sri Lanka;* orcid.org/0000-0003-0906-4441; Email: charitha.t@sliit.lk

Saravanamuthu Vigneswaran − *Faculty of Engineering, University of Technology Sydney (UTS), Broadway, NSW 2127, Australia; Faculty of Sciences & Technology (RealTek), Norwegian University of Life Sciences, Ås 1430, Norway*; Email: Saravanamuth.Vigneswaran@uts.edu.au

Authors

Leshan Usgodaarachchi − *Department of Materials Engineering, Faculty of Engineering, Sri Lanka Institute of Information Technology, Colombo 10115, Sri Lanka*

Ramanee Wijesekera − *Department of Chemistry, Faculty of Science, University of Colombo, Colombo 3 00300, Sri Lanka*

Murthi Kandanapitiye − *Department of Nano Science Technology, Wayamba University of Sri Lanka, Kuliyapitiya 60200, Sri Lanka*

Complete contact information is available at: https://pubs.acs.org/10.1021/acsomega.2c03262

Funding

This research was supported by the Accelerating Higher Education Expansion and Development (AHEAD) Operation of the Ministry of Higher Education funded by the World Bank.

Notes

The authors declare no competing financial interest.

■ ACKNOWLEDGMENTS

Authors acknowledge the Sri Lanka Institute of Nanotechnology and Industrial Technology Institute for providing the instrument facilities.

■ REFERENCES

(1) Banerjee, D.; Williams, J. C. Perspectives on Titanium Science and Technology. *Acta Mater.* **2013**, *61*, 844−879.

(2) Malczewska-Toth, B. Titanium, Zirconium, and Hafnium. In *Patty's Toxicology*; John Wiley & Sons, Inc.: Hoboken, NJ, USA, 2012; pp. 427−474, DOI: 10.1002/0471435139.tox035.pub2.

(3) Kroll, W. The Production of Ductile Titanium. *Trans. Electrochem. Soc.* **1940**, *78*, 35.

(4) Weir, A.; Westerhoff, P.; Fabricius, L.; Hristovski, K.; Von Goetz, N. Titanium Dioxide Nanoparticles in Food and Personal Care Products. *Environ. Sci. Technol.* **2012**, *46*, 2242−2250.

(5) Möllmann, A.; Gedamu, D.; Vivo, P.; Frohnhoven, R.; Stadler, D.; Fischer, T.; Ka, I.; Steinhorst, M.; Nechache, R.; Rosei, F.; Cloutier, S. G.; Kirchartz, T.; Mathur, S. Highly Compact TiO $_2$ Films by Spray Pyrolysis and Application in Perovskite Solar Cells. *Adv. Eng. Mater.* **2019**, *21*, 1801196.

(6) Gopinath, K. P.; Madhav, N. V.; Krishnan, A.; Malolan, R.; Rangarajan, G. Present Applications of Titanium Dioxide for the Photocatalytic Removal of Pollutants from Water: A Review. *J. Environ. Manage.* **2020**, *270*, No. 110906.

(7) Srikanth, B.; Goutham, R.; Badri Narayan, R.; Ramprasath, A.; Gopinath, K. P.; Sankaranarayanan, A. R. Recent Advancements in Supporting Materials for Immobilised Photocatalytic Applications in Waste Water Treatment. *J. Environ. Manage.* **2017**, *200*, 60−78.

(8) Gázquez, M. J.; Bolívar, J. P.; Garcia-Tenorio, R.; Vaca, F. A Review of the Production Cycle of Titanium Dioxide Pigment. *Mater. Sci. Appl.* **2014**, *05*, 441−458.

(9) Thambiliyagodage, C.; Wijesekera, R.; Bakker, M. G. Leaching of Ilmenite to Produce Titanium Based Materials: A Review. *Discov. Mater.* **2021**, *1*, 20.

(10) Nguyen, T. H.; Lee, M. S. A Review on the Recovery of Titanium Dioxide from Ilmenite Ores by Direct Leaching Technologies. *Mineral Processing and Extractive Metallurgy Review*. Taylor and Francis Inc. July 4, 2019, pp. 231−247.

(11) Gazquez, M. J.; Mantero, J.; Mosqueda, F.; Vioque, I.; García-Tenorio, R.; Bolívar, J. P. Radiological and Chemical Risks by Waste Scales Generated in the Titanium Dioxide Industry. *Chemosphere* **2021**, *274*, No. 129732.

(12) Hossain, S. M.; Park, H.; Kang, H. J.; Mun, J. S.; Tijing, L.; Rhee, I.; Kim, J. H.; Jun, Y. S.; Shon, H. K. Facile Synthesis and Characterization of Anatase TiO_2/g-CN Composites for Enhanced Photoactivity under UV−Visible Spectrum. *Chemosphere* **2021**, *262*, No. 128004.

(13) Mahmoud, M. H. H.; Afifi, A. A. I.; Ibrahim, I. A. Reductive Leaching of Ilmenite Ore in Hydrochloric Acid for Preparation of Synthetic Rutile. *Hydrometallurgy* **2004**, *73*, 99−109.

(14) Rajakaruna, T. P. B.; Udawatte, C. P.; Chandrajith, R.; Rajapakse, R. M. G. Nonhazardous Process for Extracting Pure Titanium Dioxide Nanorods from Geogenic Ilmenite. *ACS Omega* **2020**, *5*, 16176−16182.

(15) Verbruggen, S. W. TiO_2 Photocatalysis for the Degradation of Pollutants in Gas Phase: From Morphological Design to Plasmonic Enhancement. *J. Photochem. Photobiol., C* **2015**, *24*, 64−82.

(16) Tsang, C. H. A.; Li, K.; Zeng, Y.; Zhao, W.; Zhang, T.; Zhan, Y.; Xie, R.; Leung, D. Y. C.; Huang, H. Titanium Oxide Based Photocatalytic Materials Development and Their Role of in the Air Pollutants Degradation: Overview and Forecast. *Environ. Int.* **2019**, *125*, 200−228.

(17) Thambiliyagodage, C. Activity Enhanced TiO_2 Nanomaterials for Photodegradation of Dyes - A Review. *Environ. Nanotechnol., Monit. Manage.* **2021**, *16*, No. 100592.

(18) Seneviratne, K. L.; Munaweera, I.; Peiris, S. E.; Peiris, C. N.; Kottegoda, N. Recent Progress in Visible-Light Active (VLA) TiO_2 Nano-Structures for Enhanced Photocatalytic Activity (PCA) and Antibacterial Properties: A Review. *Iran. J. Catal.* **2021**, *11*, 217−245.

(19) Thambiliyagodage, C.; Usgodaarachchi, L. Photocatalytic Activity of N, Fe and Cu Co-Doped TiO_2 Nanoparticles under Sunlight. *Curr. Res. Green Sustainable Chem.* **2021**, *4*, No. 100186.

(20) Charitha, T.; Leshan, U.; Shanitha, M.; Ramanee, W.; Buddi, L.; Martin, B. Efficient Photodegradation Activity of α-Fe_2O_3/Fe_2TiO_5/TiO_2 and Fe_2TiO_5/TiO_2 Nanocomposites Synthesized from Natural Ilmenite. *Results Mater.* **2021**, *12*, No. 100219.

(21) Basavarajappa, P. S.; Patil, S. B.; Ganganagappa, N.; Reddy, K. R.; Raghu, A. V.; Reddy, C. V. Recent Progress in Metal-Doped TiO_2, Non-Metal Doped/Codoped TiO_2 and TiO_2 Nanostructured Hybrids for Enhanced Photocatalysis. *Int. J. Hydrogen Energy* **2020**, *45*, 7764−7778.

(22) Vargas Hernández, J.; Coste, S.; García Murillo, A.; Carrillo Romo, F.; Kassiba, A. Effects of Metal Doping (Cu, Ag, Eu) on the Electronic and Optical Behavior of Nanostructured TiO_2. *J. Alloys Compd.* **2017**, *710*, 355−363.
(23) Zheng, P.; Zhou, W.; Wang, Y.; Ren, D.; Zhao, J.; Guo, S. N-Doped Graphene-Wrapped TiO_2 Nanotubes with Stable Surface Ti3+ for Visible-Light Photocatalysis. *Appl. Surf. Sci.* **2020**, *512*, No. 144549.
(24) He, H.; Huang, D.; Pang, W.; Sun, D.; Wang, Q.; Tang, Y.; Ji, X.; Guo, Z.; Wang, H. Plasma-Induced Amorphous Shell and Deep Cation-Site S Doping Endow TiO_2 with Extraordinary Sodium Storage Performance. *Adv. Mater.* **2018**, *30*, 1801013.
(25) Eslami, A.; Amini, M. M.; Yazdanbakhsh, A. R.; Mohseni-Bandpei, A.; Safari, A. A.; Asadi, A. N,S Co-Doped TiO_2 Nanoparticles and Nanosheets in Simulated Solar Light for Photocatalytic Degradation of Non-Steroidal Anti-Inflammatory Drugs in Water: A Comparative Study. *J. Chem. Technol. Biotechnol.* **2016**, *91*, 2693−2704.
(26) Zhang, L. W.; Fu, H. B.; Zhu, Y. F. Efficient TiO_2 Photocatalysts from Surface Hybridization of TiO_2 Particles with Graphite-like Carbon. *Adv. Funct. Mater.* **2008**, *18*, 2180−2189.
(27) Karim, A. V.; Selvaraj, A. Graphene Composites in Photocatalytic Oxidation of Aqueous Organic Contaminants − A State of Art. *Process Saf. Environ. Prot.* **2021**, *146*, 136−160.
(28) Usgodaarachchi, L.; Thambiliyagodage, C. Photocatalytic Activity of GO/Fe_3O_4 Fabricated by Sri Lankan Graphite under Visible Light Irradiation. *J. Sci. Univ. Kelaniya Sri Lanka* **2021**, *14*, 51.
(29) Qi, Y.; Yang, Z.; Jiang, Y.; Han, H.; Wu, T.; Wu, L.; Liu, J.; Wang, Z.; Wang, F. Platinum-Copper Bimetallic Nanoparticles Supported on TiO_2 as Catalysts for Photo-Thermal Catalytic Toluene Combustion. *ACS Appl. Nano Mater.* **2022**, *5*, 1845−1854.
(30) AL-Jawad, S. M. H.; Taha, A. A.; Salim, M. M. Synthesis and Characterization of Pure and Fe Doped TiO_2 Thin Films for Antimicrobial Activity. *Optik* **2017**, *142*, 42−53.
(31) Bensouici, F.; Bououdina, M.; Dakhel, A. A.; Tala-Ighil, R.; Tounane, M.; Iratni, A.; Souier, T.; Liu, S.; Cai, W. Optical, Structural and Photocatalysis Properties of Cu-Doped TiO_2 Thin Films. *Appl. Surf. Sci.* **2017**, *395*, 110−116.
(32) Wang, T.; Shen, D.; Xu, T.; Jiang, R. Photocatalytic Degradation Properties of V-Doped TiO_2 to Automobile Exhaust. *Sci. Total Environ.* **2017**, *586*, 347−354.
(33) Iqbal, T.; Farman, S.; Afsheen, S.; Riaz, K. N. Novel Study to Correlate Efficient Photocatalytic Activity of WO_3 and Cr Doped TiO_2 Leading to Enhance the Shelf-Life of the Apple. *Appl. Nanosci.* **2021**, *12*, 87−99.
(34) Nigussie, G. Y.; Tesfamariam, G. M.; Tegegne, B. M.; Weldemichel, Y. A.; Gebreab, T. W.; Gebrehiwot, D. G.; Gebremichel, G. E. Antibacterial Activity of Ag-Doped TiO_2 and Ag-Doped ZnO Nanoparticles. *Int. J. Photoenergy* **2018**, *2018*, 5927485.
(35) Yang, C. C.; Wang, C. X.; Kuan, C. Y.; Chi, C. Y.; Chen, C. Y.; Lin, Y. Y.; Chen, G. S.; Hou, C. H.; Lin, F. H. Using C-Doped TiO_2 Nanoparticles as a Novel Sonosensitizer for Cancer Treatment. *Antioxidants* **2020**, *9*, 880.
(36) Katoueizadeh, E.; Zebarjad, S. M.; Janghorban, K. Synthesis and Enhanced Visible-Light Activity of N-Doped TiO_2 Nano-Additives Applied over Cotton Textiles. *J. Mater. Res. Technol.* **2018**, *7*, 204−211.
(37) Tian, H.; Shen, K.; Hu, X.; Qiao, L.; Zheng, W. N, S Co-Doped Graphene Quantum Dots-Graphene-TiO_2 Nanotubes Composite with Enhanced Photocatalytic Activity. *J. Alloys Compd.* **2017**, *691*, 369−377.
(38) Shen, K.; Xue, X.; Wang, X.; Hu, X.; Tian, H.; Zheng, W. One-Step Synthesis of Band-Tunable N, S Co-Doped Commercial TiO_2 /Graphene Quantum Dots Composites with Enhanced Photocatalytic Activity. *RSC Adv.* **2017**, *7*, 23319−23327.
(39) Helmy, E. T.; El Nemr, A.; Mousa, M.; Arafa, E.; Eldafrawy, S. Photocatalytic Degradation of Organic Dyes Pollutants in the Industrial Textile Wastewater by Using Synthesized TiO_2, C-Doped TiO_2, S-Doped TiO_2 and C,S Co-Doped TiO_2 Nanoparticles. *J. Water Environ. Nanotechnol.* **2018**, *3*, 116−127.
(40) Zhang, Y. H.; Li, Y. L.; Jiu, B. B.; Gong, F. L.; Chen, J. L.; Fang, S. M.; Zhang, H. L. Highly Enhanced Photocatalytic H_2 Evolution of Cu_2O Microcube by Coupling with TiO_2 Nanoparticles. *Nanotechnology* **2019**, *30*, 145401.
(41) Jiang, Z.; Qian, K.; Zhu, C.; Sun, H.; Wan, W.; Xie, J.; Li, H.; Wong, P. K.; Yuan, S. Carbon Nitride Coupled with CdS-TiO_2 Nanodots as 2D/0D Ternary Composite with Enhanced Photocatalytic H2 Evolution: A Novel Efficient Three-Level Electron Transfer Process. *Appl. Catal., B* **2017**, *210*, 194−204.
(42) Zhang, W.; Ma, Y.; Zhu, X.; Wang, L.; Ye, J.; Hou, X.; Liu, S.; Lu, M.; Tian, H.; Hu, X. In Situ Synthesis of α-Fe_2O_3/$LaFeO_3$ Modified with g-C_3N_4 and Ti_3C_2 for Construction of Multiple Z-Scheme/Schottky Heterojunctions as an Efficient Visible-Light Photocatalyst for Cr (VI) Reduction and Organic Pollutants Removal. *J. Alloys Compd.* **2022**, *913*, No. 165217.
(43) Avansi, W.; Catto, A. C.; Da Silva, L. F.; Fiorido, T.; Bernardini, S.; Mastelaro, V. R.; Aguir, K.; Arenal, R. One-Dimensional V_2O_5/TiO_2 Heterostructures for Chemiresistive Ozone Sensors. *ACS Appl. Nano Mater.* **2019**, *2*, 4756−4764.
(44) Fan, Z.; Meng, F.; Gong, J.; Li, H.; Hu, Y.; Liu, D. Enhanced Photocatalytic Activity of Hierarchical Flower-like CeO_2/TiO_2 Heterostructures. *Mater. Lett.* **2016**, *175*, 36−39.
(45) Li, Y.; Yang, W.; Wang, C.; Li, Z.; Lai, J.; Wang, L.; Huang, L. Achieving Controllable $Cotio_3$-Encapsulated Tio_2 Heterostructures for Enhanced Photoelectrochemical Water Splitting. *ACS Appl. Energy Mater.* **2019**, *2*, 8229−8235.
(46) Gharakhlou, A. R.; Sarvi, M. N. Synthesis of Mesoporous Nanoparticles of TiO_2 from Ilmenite. *Mater. Res. Express* **2017**, *4*, No. 025027.
(47) Samal, S. The Dissolution of Iron in the Hydrochloric Acid Leach of Titania Slag Obtained from Plasma Melt Separation of Metalized Ilmenite. *Chem. Eng. Res. Des.* **2011**, *89*, 2190−2193.
(48) Khan, R.; Javed, S.; Islam, M. Hierarchical Nanostructures of Titanium Dioxide: Synthesis and Applications. In *Titanium Dioxide - Material for a Sustainable Environment*; InTech, 2018, DOI: 10.5772/intechopen.74525.
(49) Tengvall, P.; Elwing, H.; Lundström, I. Titanium Gel Made from Metallic Titanium and Hydrogen Peroxide. *J. Colloid Interface Sci.* **1989**, *130*, 405−413.
(50) Ismail, A. A.; Bahnemann, D. W. Mesoporous Titania Photocatalysts: Preparation, Characterization and Reaction Mechanisms. *Journal of Materials Chemistry*. The Royal Society of Chemistry August 28, 2011, pp. 11686−11707.
(51) Liu, Y.; Li, X.; Sloppy, J.; Huang, Y.; Yao, P.; Yang, J.; Yang, Y. A Simple and "Green" Method for Synthesis of Magnetic Hollow Silica Spheres and Its 99Tcm Labeled Targeting Studies. *Open J. Inorg. Chem.* **2017**, *07*, 1−15.
(52) Thambiliyagodage, C.; Mirihana, S. Photocatalytic Activity of Fe and Cu Co-Doped TiO_2 Nanoparticles under Visible Light. *J. Sol-Gel Sci. Technol.* **2021**, *99*, 109−121.
(53) Jiang, Y.; Cheng, G.; Yang, R.; Liu, H.; Sun, M.; Yu, L.; Hao, Z. Influence of Preparation Temperature and Acid Treatment on the Catalytic Activity of MnO_2. *J. Solid State Chem.* **2019**, *272*, 173−181.
(54) Payormhorm, J.; Chuangchote, S.; Laosiripojana, N. CTAB-Assisted Sol-Microwave Method for Fast Synthesis of Mesoporous TiO_2 Photocatalysts for Photocatalytic Conversion of Glucose to Value-Added Sugars. *Mater. Res. Bull.* **2017**, *95*, 546−555.
(55) Roy, D.; Yadav, A. K. Green TiO_2−ZnO Nanocomposite Stimulator for the Growth of Solanum Lycopersicum in Aquaculture. *Appl. Nanosci.* **2022**, 1−21.
(56) Li, C.; Sun, T.; Zhang, D.; Zhang, X.; Qian, Y.; Zhang, Y.; Lin, X.; Liu, J.; Zhu, L.; Wang, X.; Shi, Z.; Lin, Q. Fabrication of Ternary Ag/La-Black TiO_{2-x} Photocatalyst with Enhanced Visible-Light Photocatalytic Activity for Tetracycline Degradation. *J. Alloys Compd.* **2022**, *891*, No. 161960.
(57) Yang, Z.; Qi, Y.; Wang, F.; Han, Z.; Jiang, Y.; Han, H.; Liu, J.; Zhang, X.; Ong, W. J. State-of-the-Art Advancements in Photo-

https://doi.org/10.1021/acsomega.2c03262
ACS Omega 2022, 7, 27617−27637

Assisted CO_2 Hydrogenation: Recent Progress in Catalyst Development and Reaction Mechanisms. *J. Mater. Chem. A* **2020**, *8*, 24868−24894.
(58) Keerthana, S. P.; Yuvakkumar, R.; Ravi, G.; Kumar, P.; Elshikh, M. S.; Alkhamis, H. H.; Alrefaei, A. F.; Velauthapillai, D. A Strategy to Enhance the Photocatalytic Efficiency of α-Fe_2O_3. *Chemosphere* **2021**, *270*, No. 129498.
(59) Chinnathambi, A.; Vasantharaj, S.; Saravanan, M.; Sathiyavimal, S.; Duc, P. A.; Nasif, O.; Alharbi, S. A.; Chi, N. T. L.; Brindhadevi, K. Biosynthesis of TiO_2 Nanoparticles by Acalypha Indica; Photocatalytic Degradation of Methylene Blue. *Appl. Nanosci.* **2021**, 1−8.
(60) Yin, P.; Tang, Y.; Zhang, L.; Wang, J.; Feng, X.; Dai, J. Effect of Nitric Acid Treatment on the Final Low-Frequency Microwave Absorption Performance of TiO_2/$ZnFe_2O_4$/$ZnTiO_3$ Nanocomposite. *Appl. Nanosci.* **2021**, *11*, 861−874.
(61) Liu, C.; Liu, Y.; Dang, Z.; Zeng, S.; Li, C. Enhancement of Heterogeneous Photo-Fenton Performance of Core-Shell Structured Boron-Doped Reduced Graphene Oxide Wrapped Magnetical Fe_3O_4 Nanoparticles: Fe(II)/Fe(III) Redox and Mechanism. *Appl. Surf. Sci.* **2021**, *544*, No. 148886.
(62) John Prabhahar, M.; Julyes Jaisingh, S.; Arun Prakash, V. R. Role of Magnetite (Fe_3O_4)-Titania (TiO_2) Hybrid Particle on Mechanical, Thermal and Microwave Attenuation Behaviour of Flexible Natural Rubber Composite in X and Ku Band Frequencies. *Mater. Res. Express* **2019**, *7*, No. 016106.
(63) Juang, R.-S.; Su, C.-J.; Wu, M.-C.; Lu, H.-C.; Wang, S.-F.; Sun, A.-C. Fabrication of Magnetic Fe_3O_4 Nanoparticles with Unidirectional Extension Pattern by a Facile and Eco-Friendly Microwave-Assisted Solvothermal Method. *J. Nanosci. Nanotechnol.* **2019**, *19*, 7645−7653.
(64) Hadianto, H.; Amiruddin, E.; Venera, R. S. P.; Aprilia, V. Structural and Morphological Properties of Undoped and Manganese Doped Hematite Nanoparticles Prepared by Ball Milling Method. In *Journal of Physics: Conference Series*; IOP Publishing Ltd, 2020; Vol. *1655*, p 12013, DOI: 10.1088/1742-6596/1655/1/012013.
(65) Malla, A. M.; Dar, F. A.; Shah, M. A. Influence of Precursor Concentration on Structural, Morphological and Optical Properties of Hematite (α-Fe_2O_3) Nanoparticles. *Curr. Nanomater.* **2017**, *2*, 39.
(66) Liu, Y.; Du, Y. E.; Bai, Y.; An, J.; Li, J.; Yang, X.; Feng, Q. Facile Synthesis of {101}, {010} and [111]-Faceted Anatase-TiO_2 Nanocrystals Derived from Porous Metatitanic Acid H_2TiO_3 for Enhanced Photocatalytic Performance. *ChemistrySelect* **2018**, *3*, 2867−2876.
(67) Isacfranklin, M.; Yuvakkumar, R.; Ravi, G.; Kumar, P.; Saravanakumar, B.; Velauthapillai, D.; Alahmadi, T. A.; Alharbi, S. A. Biomedical Application of Single Anatase Phase TiO_2 Nanoparticles with Addition of Rambutan (Nephelium Lappaceum L.) Fruit Peel Extract. *Appl. Nanosci.* **2020**, *11*, 699−708.
(68) Rani, C.; Pathak, D. K.; Tanwar, M.; Kandpal, S.; Ghosh, T.; Maximov, M. Y.; Kumar, R. Anharmonicity Induced Faster Decay of Hot Phonons in Rutile TiO_2 Nanorods: A Raman Spectromicroscopy Study. *Mater. Adv.* **2022**, 1602−1608.
(69) Chen, Y.; Li, J.; Li, X.; Luo, F.; Wang, Z.; Wu, L.; Li, X. Copper Oxide Nanoparticles Confined in TiO_2 Nanotubes for the Water−Gas Shift Reaction: Promotional Effect of Potassium. *J. Mater. Res.* **2021**, *36*, 4475−4484.
(70) Pérez-Pérez, L. M. C.; Báez-Rodríguez, A.; García-González, L.; Hernández-Torres, J.; Velázquez-Camilo, O.; Zamora-Peredo, L. Nanopores and Nanosheets of α-Fe_2O_3 Synthetized by Electrochemical Anodization and Analysed by Raman Spectroscopy. *MRS Adv.* **2019**, *4*, 2863−2871.
(71) Amr, R. A.; Liora Goldring-Vandergeest, I.; Liang, K.; Lok, G. H.; Hui, S.; Turak, A. Role of Hydration and Micellar Shielding in Tuning the Structure of Single Crystalline Iron Oxide Nanoparticles for Designer Applications. 2021, DOI: 10.1002/nano.202100085.
(72) Athithya, S.; Harish, S.; IKeda, H.; Shimomura, M.; Hayakawa, Y.; Archana, J.; Navaneethan, M. Hierarchically Ordered Macroporous TiO_2 Architecture via Self-Assembled Strategy for Environmental Remediation. *Chemosphere* **2022**, *288*, No. 132236.
(73) Ekoi, E. J.; Gowen, A.; Dorrepaal, R.; Dowling, D. P. Characterisation of Titanium Oxide Layers Using Raman Spectroscopy and Optical Profilometry: Influence of Oxide Properties. *Results Phys.* **2019**, *12*, 1574−1585.
(74) Thambiliyagodage, C.; Mirihana, S.; Wijesekera, R.; Madusanka, D. S.; Kandanapitiye, M.; Bakker, M. Fabrication of Fe_2TiO_5/TiO_2 Binary Nanocomposite from Natural Ilmenite and Their Photocatalytic Activity under Solar Energy. *Curr. Res. Green Sustainable Chem.* **2021**, *4*, No. 100156.
(75) Agarwal, B. K. Secondary Spectra and Satellites. 1991, 155−194, DOI: 10.1007/978-3-540-38668-1_4.
(76) Lu, L.; Wang, G.; Xiong, Z.; Hu, Z.; Liao, Y.; Wang, J.; Li, J. Enhanced Photocatalytic Activity under Visible Light by the Synergistic Effects of Plasmonics and Ti_3^+-Doping at the Ag/TiO_{2-x} Heterojunction. *Ceram. Int.* **2020**, *46*, 10667−10677.
(77) Zhao, G.; Wu, C.; Yan, M. Evolution of the Insulation Matrix and Influences on the Magnetic Performance of Fe Soft Magnetic Composites during Annealing. *J. Alloys Compd.* **2016**, *685*, 231−236.
(78) Zhao, G.; Wu, C.; Yan, M. Fabrication and Growth Mechanism of Iron Oxide Insulation Matrix for Fe Soft Magnetic Composites with High Permeability and Low Core Loss. *J. Alloys Compd.* **2017**, *710*, 138−143.
(79) Cao, Z. f.; Wen, X.; Chen, P.; Yang, F.; Ou, X. l.; Wang, S.; Zhong, H. Synthesis of a Novel Heterogeneous Fenton Catalyst and Promote the Degradation of Methylene Blue by Fast Regeneration of Fe_2^+. *Colloids Surf., A* **2018**, *549*, 94−104.
(80) Jiao, Y.; Zhang, S.; Tan, Y. Effects of Zinc−Aluminium Injection on Corrosion Behaviour and Semiconductor Properties of Carbon Steel in the PHT System of PHWR. *RSC Adv.* **2022**, *12*, 1663−1674.
(81) Zhang, D.; Hegab, H. E.; Lvov, Y.; Dale Snow, L.; Palmer, J. Immobilization of Cellulase on a Silica Gel Substrate Modified Using a 3-APTES Self-Assembled Monolayer. *Springerplus* **2016**, *5*, 48.
(82) Aware, D. V.; Jadhav, S. S. Synthesis, Characterization and Photocatalytic Applications of Zn-Doped TiO_2 Nanoparticles by Sol−Gel Method. *Appl. Nanosci.* **2016**, *6*, 965−972.
(83) Raliya, R.; Avery, C.; Chakrabarti, S.; Biswas, P. Photocatalytic Degradation of Methyl Orange Dye by Pristine Titanium Dioxide, Zinc Oxide, and Graphene Oxide Nanostructures and Their Composites under Visible Light Irradiation. *Appl. Nanosci.* **2017**, *7*, 253−259.
(84) Badli, N. A.; Ali, R.; Wan Abu Bakar, W. A.; Yuliati, L. Role of Heterojunction $ZrTiO_4$/$ZrTi_2O_6$/TiO_2 Photocatalyst towards the Degradation of Paraquat Dichloride and Optimization Study by Box−Behnken Design. *Arab. J. Chem.* **2017**, *10*, 935−943.
(85) Phattepur, H.; Siddaiah, G. B.; Ganganagappa, N. Synthesis and Characterisation of Mesoporous TiO_2 Nanoparticles by Novel Surfactant Assisted Sol-Gel Method for the Degradation of Organic Compounds. *Period. Polytech. Chem. Eng.* **2019**, *63*, 85−95.
(86) Nasi, R.; Esposito, S.; Freyria, F. S.; Armandi, M.; Gadhi, T. A.; Hernandez, S.; Rivolo, P.; Ditaranto, N.; Bonelli, B. Application of Reverse Micelle Sol−Gel Synthesis for Bulk Doping and Heteroatoms Surface Enrichment in Mo-Doped TiO_2 Nanoparticles. *Materials* **2019**, *12*, 937.
(87) Swapna, M. V.; Haridas, K. R. An Easier Method of Preparation of Mesoporous Anatase TiO_2 Nanoparticles via Ultrasonic Irradiation. 2015, *11* (7), 540−549, DOI: 10.1080/17458080.2015.1094189.
(88) Madurai Ramakrishnan, V.; Pitchaiya, S.; Muthukumarasamy, N.; Kvamme, K.; Rajesh, G.; Agilan, S.; Pugazhendhi, A.; Velauthapillai, D. Performance of TiO_2 Nanoparticles Synthesized by Microwave and Solvothermal Methods as Photoanode in Dye-Sensitized Solar Cells (DSSC). *Int. J. Hydrogen Energy* **2020**, *45*, 27036−27046.
(89) Dolgonos, A.; Mason, T. O.; Poeppelmeier, K. R. Direct Optical Band Gap Measurement in Polycrystalline Semiconductors: A Critical Look at the Tauc Method. *J. Solid State Chem.* **2016**, *240*, 43−48.
(90) Palliyaguru, L.; Kulathunga, U. S.; Jayarathna, L. I.; Jayaweera, C. D.; Jayaweera, P. M. A Simple and Novel Synthetic Route to

Prepare Anatase TiO_2 Nanopowders from Natural Ilmenite via the H_3PO_4/NH_3 Process. *Int. J. Miner. Metall. Mater.* **2020**, *27*, 846−855.
(91) Santos, E.; Catto, A. C.; Peterline, A. F.; Avansi, W., Jr. Transition Metal (Nb and W) Doped TiO_2 Nanostructures: The Role of Metal Doping in Their Photocatalytic Activity and Ozone Gas-Sensing Performance. *Appl. Surf. Sci.* **2022**, *579*, No. 152146.
(92) Gunathilaka, H.; Thambiliyagodage, C. J.; Usgodaarachchi, L.; Thambiliyagodage, C.; Usgodaarchchi, L.; Angappan, S. Effect of Surfactants on Morphology and Textural Parameters of Silica Nanoparticles Derived from Paddy Husk and Their Efficient Removal of Methylene Blue Synthesis and Characterization of Novel Nanomaterials for Removal of Textile Dyes in Industrial Wastewater View Project Effect of Surfactants on Morphology and Textural Parameters of Silica Nanoparticles Derived from Paddy Husk and Their Efficient Removal of Methylene Blue. 2021, DOI: 10.6084/m9.figshare.14904873.
(93) Usgodaarachchi, L.; Thambiliyagodage, C.; Wijesekera, R.; Bakker, M. G. Synthesis of Mesoporous Silica Nanoparticles Derived from Rice Husk and Surface-Controlled Amine Functionalization for Efficient Adsorption of Methylene Blue from Aqueous Solution. *Curr. Res. Green Sustainable Chem.* **2021**, *4*, No. 100116.
(94) Thambiliyagodage, C.; Usgodaarachchi, L. Efficient Removal of Methylene Blue by Turbostratic Carbon/Fe3C/Fe Composite Synthesized by Catalytic Graphitization of Sucrose. *Mater. Today Proc.* **2022**, *56*, 2189−2194.
(95) Zahoor, M.; Arshad, A.; Khan, Y.; Iqbal, M.; Bajwa, S. Z.; Soomro, R. A.; Ahmad, I.; Butt, F. K.; Iqbal, M. Z.; Wu, A.; Khan, W. S. Enhanced Photocatalytic Performance of CeO2−TiO2 Nanocomposite for Degradation of Crystal Violet Dye and Industrial Waste Effluent. *Appl. Nanosci.* **2018**, *8*, 1091−1099.
(96) Parmar, A.; Kaur, G.; Kapil, S.; Sharma, V.; Sharma, S. Biogenic PLGA-Zinc Oxide Nanocomposite as Versatile Tool for Enhanced Photocatalytic and Antibacterial Activity. *Appl. Nanosci.* **2019**, *9*, 2001−2016.
(97) Lou, Z.; Li, Y.; Song, H.; Ye, Z.; Zhu, L. Fabrication of Fe_2TiO_5/TiO_2 Nanoheterostructures with Enhanced Visible-Light Photocatalytic Activity. *RSC Adv.* **2016**, *6*, 45343−45348.
(98) Kumar, A.; Kumar, A.; Sharma, G.; Al-Muhtaseb, A. H.; Naushad, M.; Ghfar, A. A.; Stadler, F. J. Quaternary Magnetic BiOCl/g-$C_3N_4/Cu_2O/Fe_3O_4$ Nano-Junction for Visible Light and Solar Powered Degradation of Sulfamethoxazole from Aqueous Environment. *Chem. Eng. J.* **2018**, *334*, 462−478.
(99) Chen, K.; Dao, T. D.; Ngo, T. D.; Ngo, H. D.; Tamanai, A.; Ishii, S.; Li, X.; Misawa, H.; Nagao, T. Enhanced Photocurrent Generation from Indium−Tin-Oxide/Fe_2TiO_5 Hybrid Nanocone Arrays. *Nano Energy* **2020**, *76*, No. 104965.
(100) kumar, R. R.; Raj, R.; Venimadhav, A. Weak Ferromagnetism in Band-Gap Engineered α-$(Fe_2O_3)_{1-X}(Cr_2O_3)X$ Nanoparticles. *J. Magn. Magn. Mater.* **2019**, *473*, 119−124.
(101) Devaraji, P.; Gao, R.; Xiong, L.; Jia, X.; Huang, L.; Chen, W.; Liu, S.; Mao, L. Usage of Natural Leaf as a Bio-Template to Inorganic Leaf: Leaf Structure Black TiO_2/CdS Heterostructure for Efficient Photocatalytic Hydrogen Evolution. *Int. J. Hydrogen Energy* **2021**, *46*, 14369−14383.
(102) Jiménez-Calvo, P.; Caps, V.; Keller, V. Plasmonic Au-Based Junctions onto TiO_2, GC_3N_4, and TiO_2-GC_3N_4 Systems for Photocatalytic Hydrogen Production: Fundamentals and Challenges. *Renew. Sustainable Energy Rev.* **2021**, *149*, No. 111095.
(103) Roldan, A.; Santos-Carballal, D.; De Leeuw, N. H. A Comparative DFT Study of the Mechanical and Electronic Properties of Greigite Fe_3S_4 and Magnetite Fe_3O_4. *J. Chem. Phys.* **2013**, *138*, 204712.
(104) Liu, H.; Di Valentin, C. Band Gap in Magnetite above Verwey Temperature Induced by Symmetry Breaking. *J. Phys. Chem. C* **2017**, *121*, 25736−25742.
(105) Odkhuu, D.; Taivansaikhan, P.; Yun, W. S.; Hong, S. C. A First-Principles Study of Magnetostrictions of Fe_3O_4 and $CoFe_2O_4$. *J. Appl. Phys.* **2014**, *115*, 17A916.
(106) Lee, R. B.; Juan, J. C.; Lai, C. W.; Lee, K. M. Ilmenite: Properties and Photodegradation Kinetic on Reactive Black 5 Dye. *Chin. Chem. Lett.* **2017**, *28*, 1613−1618.
(107) Lubis, S.; Maulana, I. M. SYNTHESIS AND CHARACTERIZATION OF TiO_2/α-Fe_2O_3 COMPOSITE USING HEMATITE FROM IRON SAND FOR PHOTODEGRADATION REMOVAL OF DYE. *J. Nat.* **2018**, *18*, 38−43.
(108) Lee, R. B.; Lee, K. M.; Lai, C. W.; Pan, G. T.; Yang, T. C. K.; Juan, J. C. The Relationship between Iron and Ilmenite for Photocatalyst Degradation. *Adv. Powder Technol.* **2018**, *29*, 1779−1786.
(109) Hamza, A.; Ozaki, Y.; Galadima, M. S. Photocatalytic Degradation of Methylene Blue Using Natural Ilmenite Upgraded via HCl Leaching: Modelling and Optimization. *Appl. J. Environ. Eng. Sci.* **2019**, *5*, 252−262.
(110) Mafa, P. J.; Swana, U. S.; Liu, D.; Gui, J.; Mamba, B. B.; Kuvarega, A. T. Synthesis of Bi5O7I-MoO_3 Photocatalyst via Simultaneous Calcination of BiOI and MoS_2 for Visible Light Degradation of Ibuprofen. *Colloids Surf., A* **2021**, *612*, No. 126004.
(111) Kordestani, B.; Jalilzadeh Yengejeh, R.; Takdastan, A.; Neisi, A. K. A New Study on Photocatalytic Degradation of Meropenem and Ceftriaxone Antibiotics Based on Sulfate Radicals: Influential Factors, Biodegradability, Mineralization Approach. *Microchem. J.* **2019**, *146*, 286−292.
(112) Ramaswamy, P.; Devkota, S.; Pokharel, R.; Nalamati, S.; Stevie, F.; Jones, K.; Reynolds, L.; Iyer, S. A Study of Dopant Incorporation in Te-Doped GaAsSb Nanowires Using a Combination of XPS/UPS, and C-AFM/SKPM. *Sci. Reports* **2021**, *11*, 1−14.
(113) AlSalka, Y.; Granone, L. I.; Ramadan, W.; Hakki, A.; Dillert, R.; Bahnemann, D. W. Iron-Based Photocatalytic and Photoelectrocatalytic Nano-Structures: Facts, Perspectives, and Expectations. *Appl. Catal., B* **2019**, *244*, 1065−1095.
(114) Khan, A. A.; Tahir, M.; Bafaqeer, A. Constructing a Stable 2D Layered Ti_3C_2MXene Cocatalyst-Assisted TiO_2/g-C_3N_4/Ti_3C_2Heterojunction for Tailoring Photocatalytic Bireforming of Methane under Visible Light. *Energy Fuels* **2020**, *34*, 9810−9828.

https://doi.org/10.1021/acsomega.2c03262
ACS Omega 2022, 7, 27617−27637